



# Dynamic modeling, simulation, and MIMO predictive control of a tubular solid oxide fuel cell

Benjamin J. Spivey, Thomas F. Edgar\*

Department of Chemical Engineering, The University of Texas at Austin, 1 University Station C0400, Austin, TX 78712, USA

## ARTICLE INFO

### Article history:

Received 15 June 2011

Received in revised form 11 January 2012

Accepted 24 January 2012

Available online 3 March 2012

### Keywords:

Multi-input multi-output

Model predictive control

Distributed parameter models

Solid oxide fuel cell

Dynamic simulation

Nonlinear programming

## ABSTRACT

Solid oxide fuel cells are a promising option for distributed energy stationary power generation that offers efficiencies up to 50% in stand-alone applications, 70% in hybrid gas turbine applications and 80% in cogeneration. To advance SOFC technology sufficiently for widespread market penetration, the SOFC must demonstrate improved cell lifetime from the status quo. Much research has been performed to improve SOFC lifetime using advanced geometries and materials, and in this research, we suggest further improving lifetime by designing an advanced control algorithm based upon preexisting mechanical stress analysis [1]. Control algorithms commonly address SOFC lifetime related operability objectives using unconstrained, SISO control algorithms that seek to minimize thermal transients. While thermal fatigue may be one thermal stress driver, these studies often do not consider maximum radial thermal gradients or critical absolute temperatures in the SOFC. In addition, researchers often discuss hot-spots as a critical lifetime reliability issue, but as previous stress work demonstrates, the minimum cell temperature is the primary thermal stress driver in tubular SOFCs modeled after the Siemens Power Generation, Inc. design. In this work, we present a dynamic, quasi-two-dimensional model for a high-temperature tubular SOFC combined with ejector and prereformer models. The model captures dynamics of critical thermal stress drivers and is used as the physical plant for closed-loop simulations with a constrained, MIMO model predictive control algorithm. Closed-loop simulation results demonstrate effective load-following, operability constraint satisfaction, and disturbance rejection.

© 2012 Elsevier Ltd. All rights reserved.

## 1. Introduction

Solid oxide fuel cell (SOFC<sup>1</sup>) systems are ideal candidates for stationary power generation in central plant and distributed energy applications due to demonstrated high efficiencies, low environmental and noise emissions, and potential for various balance of plant configurations [2–4]. Stand-alone SOFC systems have demonstrated efficiencies ranging from 40 to 50% at capacities of 1 kWe and higher and efficiencies from 60 to 70% for pressurized hybrid gas turbine–solid oxide fuel cell (GT–SOFC) systems. Combining the SOFC prime mover with downstream users of thermal energy into a combined heat and power (CHP) system increases overall efficiency to approximately 80% [5]. SOFC systems release a high temperature effluent gas ranging from 600 to 1000 °C thereby permitting (1) internal reformation of fuels such as natural gas and (2) potential for a variety of CHP applications and combined cycles. In addition,

the SOFC redox mechanism is capable of oxidizing carbon monoxide, thereby preventing CO poisoning and further enabling usage of syngas. Despite apparent advantages, SOFCs have not been adopted as a mainstream power generation technology due primarily to challenges of meeting lifetime and availability goals, manufacturing cost, and operational flexibility for load following. The lifetime and operational flexibility goals can be directly addressed with a fundamental understanding of system dynamics and controls, and overall cost is indirectly related to the latter goals through extended lifetime.

Solid oxide fuel cells are electrochemical energy conversion devices that operate by oxidizing hydrogen and carbon monoxide at the anode and reducing oxygen at the cathode. Oxygen anions, as the charge-transport species, migrate across the electrolyte from cathode to anode and react with oxidized fuel species to produce carbon dioxide and water. Single tubular cells produce power in the range of 100 W and are combined in series into bundles and stacks that may contain thousands of cells. Due to high operating temperatures, fuel mixtures containing methane may be sent directly to the anode surface with methane undergoing direct internal reformation. Excess thermal heat may also be utilized for indirect internal reformation with enclosed reformers in proximity to the fuel cell stack. The dynamic response of an SOFC

\* Corresponding author. Tel.: +1 512 471 3080; fax: +1 512 471 7060.

E-mail address: [edgar@che.utexas.edu](mailto:edgar@che.utexas.edu) (T.F. Edgar).

<sup>1</sup> SOFC: solid oxide fuel cell; CHP: combined heat and power; SECA: Solid State Energy Conversion Alliance; CTQ: critical-to-quality per Six Sigma; SCR: steam-to-carbon ratio; QSS: quasi-steady-state; LHV: lower heating value

is characterized by time constants ranging from milliseconds for electrical transport, tenths of seconds for mass transport, and minutes to hours for thermal transport. Dynamic operation contains phenomena representative of numerator dynamics and nonlinear, multivariable interactions between manipulated and controlled variables.

Despite the benefits of SOFC power generation for distributed energy, challenges must be solved before SOFCs experience widespread adoption in energy markets. Manufacturing cost of the SOFC has been one limiting factor. SOFC stack manufacturing cost is reported by the Solid State Energy Conversion Alliance (SECA) as greater than \$1500/kW at the outset of the SECA collaboration in 2000 with the goal of reducing stack cost to \$175/kW to provide an overall power generation cost of \$700/kW by 2012 (2007 dollar basis) [6]. Reported SOFC lifetimes have yet to reach SECA design life goals of greater than 40,000 h. As of Q1 2009 Siemens reported a successful completion of a 5000 h stack test on the Delta 8 R0 SOFC and plans to complete at 25,000 h stack test on a Delta 8 “MWe-class” module by Q3 2015 [7]. SOFC are susceptible to many modes of failure and degradation ranging from microcracking, delamination, corrosion, redox material degradation, and catalyst poisoning; thermomechanical stress is a primary driver of SOFC failure and degradation. In order to meet the SECA requirements, the fuel cell community recognizes the importance of a fundamental understanding of fuel cell dynamics regarding the operability critical-to-quality (CTQ) variables – steam-to-carbon ratio, thermal gradients, local temperatures, and fuel/air utilizations [8]. Researchers investigating drivers of thermomechanical stress and microcracking in tubular SOFC have emphasized the importance of advanced control to prevent excursions into unsafe operating regimes [1].

SOFC controls literature have proposed PID control, optimal control, and various model-based control solutions, and the proposed controllers commonly are single-input single-output (SISO) or multi-input single-output (MISO) [9–12]. One case of multi-input multi-output (MIMO) MPC is shown when Jurado developed a controller for power and terminal voltage using current and fuel flow as manipulated variables using a Hammerstein model [13]. In this application Jurado demonstrated that the integrated time averaged error is ten-percent lower for MPC than PI controllers. Mueller and Junker demonstrated a MIMO linear quadratic regulator (LQR) to control power, lumped cell temperature, combustor temperature, voltage, and gas turbine shaft speed. While the fuel cell temperature variation is mitigated by the controller, they suggest additional research on advanced control is needed, and the mean temperature demonstrates an upward drift for large step changes [14]. When minimizing thermal stresses is a control objective, researchers often seek to minimize variation of a nominal stack temperature using a lumped fuel cell model or outlet gas temperature [9–12,14,15]. A couple researchers have also sought to control thermomechanical stress indirectly by minimizing voltage variation using predictive control techniques [13,16]. These techniques may reduce the need for instrumentation or soft sensors but do not capture lifetime CTQ variables directly. Seume investigated key drivers for thermomechanical stress in a cathode-supported tubular SOFC and concluded that the minimum cell temperature and maximum radial thermal gradient are the primary contributors to tensile stresses in tubular SOFC [1]. Axial gradients and positive radial gradients had negligible contributions to tensile stress in comparison. The minimum cell temperature is a primary driver for stress since the zero-stress state exists at the sintering temperature around 1250 °C. The SOFC design has a close interaction with control objectives. While lifetime operability variables may be different for planar SOFCs, the same conclusion applies that these controlled variables should be based on lifetime stress analysis.

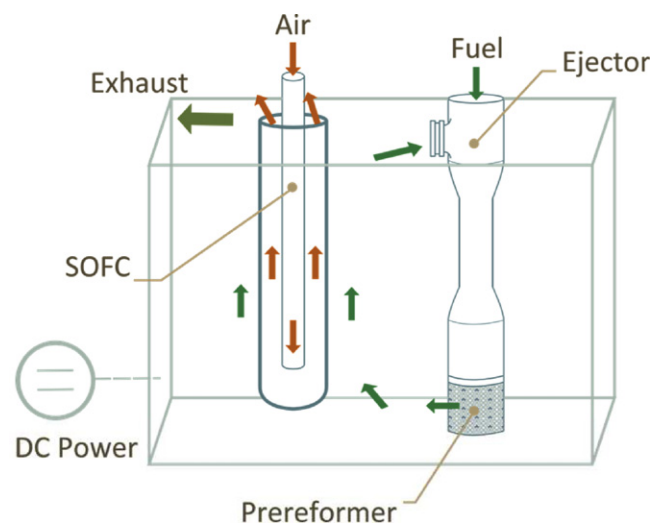


Fig. 1. Internal fuel and air flow within the SOFC system.

A thorough review of state of the art SOFC controls research indicates that additional research is needed to answer critical questions regarding the following:

- suitability of a lumped stack temperature, or outlet gas temperature, as a CV to minimize thermal tensile stress
- identifying advantages of constrained control for SOFC operation
- investigating multivariable interactions and nonlinearity for SOFC MVs and CVs.

The presented research in this paper seeks to address these issues regarding SOFC dynamics and control. Dynamic simulations and control results are based on using a dynamic, quasi-two-dimensional, differential-and-algebraic (DAE) model for the cathode-supported tubular SOFC originally designed by Siemens Westinghouse. The Siemens Westinghouse design is chosen as a simulation test-bed due to the comparatively greater amount of publically available validation data. The dynamic SOFC model solves simultaneously with a prereformer and ejector model as a combined SOFC system model in MATLAB/Simulink and using APMonitor/APOPT as a language/solver for the SOFC dynamic submodel. A linear model predictive control (MPC) algorithm is developed as a nonlinear programming problem and solved using MATLAB *fmincon*. The MPC algorithm comprises a nonlinear objective function subject to hard constraints on manipulated variables and soft constraints on controlled variables. Results for SOFC control in the presence of fuel quality disturbances demonstrate that the load may be maintained subject to  $\pm 10\%$  methane concentration variation.

## 2. SOFC system modeling

Solid oxide fuel cell models have been developed for many applications; material design and selection, feature design, system design, operational strategies, and component selection are the primary applications. The present model is designed to provide insight into overall fuel cell system design and operational and control strategies along with insight into internal phenomena.

The standard tubular solid oxide fuel cell system, modeled after the Siemens Power Generation, Inc. design, contains an SOFC stack, ejector, and prereformer as shown in Fig. 1. Full or partial load operation of the SOFC requires (1) a constant fuel input to the ejector, which may consist of fuels including natural gas, ethanol, and hydrogen, (2) desulfurized SOFC inlet fuel with hydrocarbons

reformed to methane, hydrogen, or carbon monoxide, (3) recirculation of steam from the SOFC outlet through the ejector back to the SOFC inlet, (4) preheated air and fuel, and (5) an external electrical circuit. Typical systems will also have a combustor to consume effluent methane and hydrogen.

The SOFC system-level model presented here comprises three submodels with transport delays between the submodels. A tubular SOFC submodel, ejector submodel, and prereformer submodel are connected within Simulink to form the SOFC system-level model; submodels are solved sequentially at each time interval. Internal system model variables exchanged between the submodels are gas transport states of temperature and molar flow for the SOFC and temperature, mass flow, and mole concentration for the ejector and prereformer. A gas transport delay block is applied to inlet variables of all submodels.

The SOFC system model presented here differs from many existing SOFC models in several key aspects. The SOFC submodel, as a two-dimensional, distributed parameter model, provides resolution in both axial and radial directions. The two-dimensional model provides more accurate dynamics and input–output relationships than a lumped model for the tubular SOFC; both of which are important for controls studies. The system model contains all prime mover elements of the standard Siemens Power Generation tubular SOFC system, fuel cell, ejector, and prereformer, to ensure that the manipulated variables (MVs) can be changed with standard equipment. The objective of the present system model is to investigate control of SOFC fuel cell reliability in the presence of load-following and fuel quality disturbances. As such, it does not contain some features found in lumped SOFC models in literature, such as electrical balance of plant or gas turbines.

The available manipulated variables for the SOFC system are inlet fuel pressure and temperature, cell voltage, inlet air mass flow and temperature, and system pressure as changed by the air compressor. The inlet fuel pressure and temperature are connected to the ejector submodel, and all other MVs are connected to the fuel cell submodel. The manipulated variables may be changed by balance of plant equipment. The fuel and air temperatures may be changed with recuperators and bypass control valves. Fuel pressure, air mass flow, and system pressure may be changed with variable speed compressors. Cell voltage may be changed via the electrical regulatory controls.

Controlled variables (CVs) for the system are the power, minimum cell temperature, maximum radial thermal gradient, air utilization, fuel utilization, steam-to-carbon ratio (SCR), and efficiency. The SCR is calculated from the ejector submodel, and all other CVs are calculated from the fuel cell model. These CVs are chosen to satisfy performance criteria of load-following and efficiency and lifetime criteria. Power is the only tracking CV. All of the operability CVs – temperatures, utilizations, and SCR – may be satisfied by limit constraints; some recent SOFC literature has chosen temperature as a tracking CV in the absence of predictive control [17]. Efficiency is a CV to be maximized although this is a lower priority than power or operability objectives. Since the number of CVs is greater than MVs, including all of the CVs will result in a *thin plant* case regardless of whether the controller structure is centralized or decentralized. If SOFC system operation is sufficiently far from at least one CV constraint in this case, the controller will effectively act like the *square* or *fat plant* case [18]. The SOFC submodel is modeled dynamically while the ejector and prereformer submodels are modeled as quasi-steady-state (QSS) since only gas properties are considered in these latter two submodels. In the same manner gas transport in the SOFC submodel is modeled as QSS. The three transport delay models account for gas phase transport delays.

The dynamic changes modeled for the SOFC system are electrical load setpoint changes and inlet fuel concentration disturbance changes. The electrical load setpoint is determined by the

electrical grid demand; the variance of electrical load will depend on how the configuration of the SOFC system with energy storage and the grid. As the SOFC source fuel is natural gas, the fuel quality can be expected to vary in methane concentration, particularly in unconventional applications such as landfills or biofuel plants. The mean concentration of CH<sub>4</sub> in unprocessed natural gas can be considered to be ninety-five-percent [19] though this figure may vary significantly, and the remainder of fuel may contain CO, CO<sub>2</sub>, N<sub>2</sub>, and H<sub>2</sub>O. Natural gas is commonly known to contain hydrogen sulfide, and this impurity is expected to be removed by upstream processing to negligible concentrations. Current and voltage disturbances are expected to be handled by an external DC converter controller and are thus not considered in this model. Ambient temperature would be a disturbance if the air or fuel temperatures were not considered as MVs.

### 2.1. Tubular SOFC submodel

The solid oxide fuel cell models may have differing steady-state assumptions, discretization, and constants to suit the model purpose. Common modeling objectives are fuel cell design, system balance of plant design, steady-state and dynamic operational knowledge, and control studies. The dynamic model as developed here has three primary objectives: (1) investigating the dynamic response of important controlled variables subject to disturbances; (2) testing advanced control strategies; and (3) optimizing the system size and inlet variables. In consideration of these objectives, the computational model is designed as follows:

- A two-dimensional, distributed parameter model calculates fuel cell intermediate variables and state variables spatially in the axial and radial directions. Symmetry is assumed in the circumferential direction.
- A finite-volume approach ensures conservation of energy between adjacent nodes.
- The single cell-level model exists within the stack center and assumes no net heat exchange between cells, end-effects, or heat exchange with the environment.
- The air and fuel chambers may contain up to seven chemical species: H<sub>2</sub>, H<sub>2</sub>O, O<sub>2</sub>, N<sub>2</sub>, CH<sub>4</sub>, CO, and CO<sub>2</sub>.
- Temperature-critical properties are modeled as a function of temperature: the air and fuel specific heat capacities, solid thermal resistance of each electrode–electrolyte assembly (EEA) layer, reaction constants, Nernst voltage, and polarization losses.
- Concentric tube radiation occurs between the air supply tube and cathode surface.
- The steam reformation endothermic heat generation term is a surface reaction on the outer diameter of the anode, and the electrochemical exothermic heat generation term is a volumetric reaction within the electrolyte.
- The fuel and air chamber has uniform pressure with the pressure calculated based upon Bernoulli's equation with an additional viscous head loss.
- Current flow occurs in the circumferential direction but not longitudinal due to equipotential voltage. The electrochemical reaction considers hydrogen as the fuel reactant.
- The dynamic model time update is sufficiently long, one second, such that the quasi-steady-state assumption for electrical and gas transport dynamics is valid.

A cross-section demonstrating the two-dimensional model is shown in Fig. 2 with a single finite volume having an axial length of  $\Delta x$ . Each unique fuel cell layer is modeled with one finite volume in the radial direction; the fuel cell layers are listed as follows: the supply tube air chamber, supply tube solid, cathode air chamber, cathode solid, electrolyte solid, anode solid, and anode air chamber.

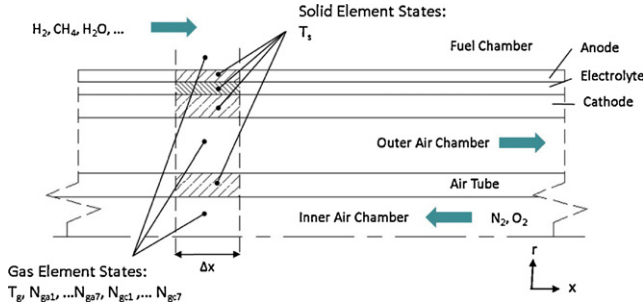


Fig. 2. The SOFC cross-section illustrates the 7 finite volumes in the radial direction (not to scale).

Each radial layer is discretized in the axial direction with forty volumes for the steady-state model and ten volumes in the dynamic model.

The solid oxide fuel cell submodel requires inputs from the reformer submodel within the fuel cell system and the external MVs. The available SOFC external MVs are mass flow and temperature of inlet air, system pressure, and the equipotential cell voltage. The voltage can be changed practically by adjusting external resistance via the power conversion equipment. Output variables from the fuel cell are the outlet gas temperature and molar concentrations for both fuel and air streams, minimum electrolyte temperature, electrolyte temperature distribution, maximum EEA radial thermal gradient, current, power, efficiency, fuel utilization, and air utilization.

### 2.1.1. Material balance

The conservation of species is accounted by performing a QSS mole-basis material balance for each gas volume in the axial direction. Open-loop tubular SOFC gas dynamic response settles within less than 1 s for step changes of 0.1–0.2 V and 10–14% of fuel flow rate at the considered nominal value [8]. The species balance is calculated according to Eq. (1) as follows:

$$\dot{N}_{i,out} = \dot{N}_{i,in} + \sum_{j=1}^3 v_i r_j \quad [\text{mol/s}] \quad (1)$$

where  $\dot{N}_i$  is the species molar flow rate in mol/s,  $v_i$  is the stoichiometric coefficient,  $r_j$  is the reaction rate in mol/s,  $i$  refers to the species, and  $j$  refers to the reaction. The species considered are  $\text{H}_2$ ,  $\text{H}_2\text{O}$ ,  $\text{O}_2$ ,  $\text{N}_2$ ,  $\text{CH}_4$ ,  $\text{CO}$ , and  $\text{CO}_2$ . The three reaction terms for the fuel chamber are steam reformation, water–gas shift, and electrochemical reactions.

### 2.1.2. Reformation and shift reactions

The reaction expressions for methane reformation and water–gas shift reactions are shown respectively in Eq. (2).



Due to SOFC high-temperature operation in excess of 600 °C, fuel may be reformed directly along the anode surface. A fuel mixture primarily consisting of methane, hydrogen, and steam is considered as the fuel at the anode inlet in a similar manner as Campanari and Aguiar [20,21]. Tubular reaction models commonly use an area-based methane reformation model [22,23]. The model chosen here is based upon the empirical equation proposed by Achenbach and Riensche [24] which is first-order in methane partial pressure for

a 80 wt.%  $\text{ZrO}_2$  and 20 wt.% Ni cermet; the reaction expression is shown as follows in Eq. (3):

$$r_{\text{CH}_4} = A \exp\left(-\frac{E_a}{RT}\right) p_{\text{CH}_4} \quad [\text{mol m}^{-1} \text{s}^{-1}], \quad (3)$$

with the frequency factor  $A$ , activation energy  $E_a$ , gas constant  $R$ , anode temperature  $T$ , and methane partial pressure  $p_{\text{CH}_4}$ . The frequency factor and activation energy were found empirically by the same authors as follows in Eq. (4):

$$\begin{aligned} A &= 4274 \quad [\text{mol m}^{-2} \text{bar}^{-1} \text{s}^{-1}] \\ E_a &= 82 \quad [\text{kJ mol}^{-1}]. \end{aligned} \quad (4)$$

The water–gas shift reaction is commonly considered to be at equilibrium since it reaches completion very quickly at high temperatures greater than 600 °C at which catalysts are typically not used. The expression for the shift reaction is shown as follows in Eq. (5):

$$r_{\text{shift}} = k \left( X_{\text{H}_2\text{O}} X_{\text{CO}} - \frac{X_{\text{H}_2} X_{\text{CO}_2}}{K_{\text{eq}}} \right) \quad [\text{mol m}^{-3} \text{s}^{-1}], \quad (5)$$

with the mole fractions denoted by  $X$ , pre-exponential factor  $k$ , and equilibrium constant  $K_{\text{eq}}$ . The pre-exponential factor may be chosen heuristically to ensure the shift reaction proceeds to completion. The equilibrium constant is calculated via an empirical equation as follows in Eq. (6):

$$\begin{aligned} K_{\text{eq}} &= \exp(-0.2935\zeta^3 + 0.635\zeta^2 + 4.1788\zeta + 0.3169) \\ \zeta &= \frac{1000}{T} - 1. \end{aligned} \quad (6)$$

where the temperature  $T$  is in Kelvin [25].

### 2.1.3. Electrochemical equations

The primary electrochemical reaction within the SOFC is hydrogen oxidation which is composed of two half-reactions occurring at the anode and cathode respectively as shown in Eq. (7). The two half-reactions are followed by the combined redox reaction.



The open-circuit voltage is calculated using the Nernst equation as a combination of (1) the reference voltage at standard pressure and unity activity and (2) a term dependent upon local reactant–product partial pressures and cell temperature as shown in Eq. (8):

$$\begin{aligned} V_{\text{oc}} &= V_{\text{H}_2}^0 + \frac{RT}{2F} \ln \left( \frac{p_{\text{H}_2} p_{\text{O}_2}^{0.5}}{p_{\text{H}_2\text{O}}} \right) \\ V_{\text{H}_2}^0 &= -\frac{\Delta G_0}{2F} + \frac{\Delta S_0}{2F} (T - 298) \end{aligned} \quad (8)$$

with the open-circuit voltage  $V_{\text{oc}}$ , reference voltage  $V_{\text{H}_2}^0$ , universal gas constant  $R$ , Faraday's constant  $F$ , partial pressures  $p_i$  in bar, and temperature  $T$  in Kelvin. Values for constants within the Nernst equation may be readily found in literature [26].

The actual cell voltage  $V_{\text{cell}}$  is calculated as the difference between open-circuit voltage and polarization losses, or overpotential, as shown in Eq. (9):

$$V_{\text{cell}} = V_{\text{oc}} - \eta_{\text{act}} - \eta_{\text{conc}} - \eta_{\text{ohm}}, \quad (9)$$

with activation losses  $\eta_{\text{act}}$ , concentration losses  $\eta_{\text{conc}}$ , and ohmic losses  $\eta_{\text{ohm}}$ . The concentration, or diffusion, overpotential is neglected in some literature since it is orders of magnitude below the activation and ohmic losses in the primary operating range; other literature have set the loss equal to 50 mV [27]. Whereas the losses and open-circuit voltage are locally dependent, the cell



voltage is commonly considered to be constant across the fuel cell length; this is commonly known as the equipotential assumption.

The current-collector, anode, electrolyte, and cathode contribute to conductive resistance, and ohmic loss is calculated via Ohm's law as shown in Eq. (10):

$$\eta_{ohm} = IR_{ohm}, \quad (10)$$

with finite volume current  $I$  in amps and volume resistance  $R_{ohm}$  in ohms. EEA layer resistances are calculated based upon published expressions for thermal conductivity as a function of temperature [22].

Activation overpotential represents the effect of electrode half-reaction kinetics. Proceeding with the electrochemical reaction requires overcoming an activation energy barrier thereby causing a voltage drop. The activation overpotential is calculated via the Butler–Volmer relations as shown in Eq. (11):

$$i = i_0 \left[ \exp \left( \beta \frac{nF\eta_{act}}{RT} \right) - \exp \left[ - (1 - \beta) \frac{nF\eta_{act}}{RT} \right] \right] \quad [\text{A m}^{-2}], \quad (11)$$

with the current density  $i$ , exchange current density  $i_0$ , electronic transfer coefficient  $\beta$ , and the number of electrons involved in the half-reaction  $n$  [28]. For low activation overpotential conditions, the Butler–Volmer relation in Eq. (11) may be approximated by a linear relation as shown in Eq. (12):

$$\eta_{act} = \frac{RTi}{nFi_0}. \quad (12)$$

The exchange current density is calculated as a function of local partial pressures and cell temperature as shown in Eq. (13):

$$\begin{aligned} i_{0,an} &= \gamma_{an} \left( \frac{p_{H_2}}{p_{amb}} \right) \left( \frac{p_{H_2O}}{p_{amb}} \right)^m \exp \left( -\frac{E_{act,an}}{RT} \right) \quad [\text{A m}^{-2}], \\ i_{0,cat} &= \gamma_{cat} \left( \frac{p_{O_2}}{p_{amb}} \right)^{0.25} \exp \left( -\frac{E_{act,an}}{RT} \right) \quad [\text{A m}^{-2}], \end{aligned} \quad (13)$$

with the values for all constants as found in literature [22,28].

Concentration overpotential, or diffusion overpotential, is included in the voltage polarization losses to compensate for voltage losses resulting when the reaction site concentration is lower than the bulk concentration due to diffusion mass transfer. The overall diffusion overpotential is calculated as the sum of anodic and cathodic overpotentials as shown in Eq. (14):

$$\eta_{conc} = \eta_{conc,an} + \eta_{conc,cat} = \frac{RT}{2F} \ln \left( \frac{X_{H_2}^b X_{H_2O}^r}{X_{H_2}^r X_{H_2O}^b} \right) + \frac{RT}{4F} \ln \left( \frac{X_{O_2}^b}{X_{O_2}^r} \right), \quad (14)$$

with the molar fractions  $X$  for bulk  $b$  and reaction  $r$  site locations. Within the operating range less than peak SOFC power, the ohmic and activation losses are orders of magnitude greater than the concentration overpotential. Expressions for the mole fractions at reaction sites are derived by applying Fick's law. An expression for the molar flux of hydrogen is shown in Eq. (15):

$$\begin{aligned} J_{H_2} &= -\frac{p_{an}D}{RT} \frac{dX_{H_2}}{J_{tot}} + X_{H_2} J_{tot} \quad [\text{mol m}^{-2}] \\ J_{tot} &= J_{H_2} + J_{H_2O} = 0 \quad [\text{mol m}^{-2}] \end{aligned} \quad (15)$$

with the molar flux of hydrogen  $J_{H_2}$  and the total molar flux  $J_{tot}$  being equal to zero since the steam flux is equal and opposite the hydrogen flux. This expression can be integrated over the two diffusion steps, from the bulk to local electrode concentration and from the local to reaction site concentration. A complete description of equations needed to calculate the concentration overpotential is given by Campanari [22].

#### 2.1.4. Ohmic resistance

Given the equipotential assumption, current flow within the fuel cell is contained within the circumferential and radial directions and is driven by radial potential gradients [28]. The overall ohmic resistance is calculated as the combination of individual layer resistances as a function of temperature, in the same manner as other published literature [22].

The tubular SOFC cross-section is discretized circumferentially and radially into volumes of  $45^\circ$  segments, and resistance for volumetric segment  $i$  may be calculated from the resistivity as shown in Eq. (16):

$$R_i = \frac{\rho_i \delta_i}{A_i} \quad [\Omega], \quad (16)$$

with the thickness  $\delta$  calculated as the length in the direction of electrical transport, and the area  $A$  is the area of electrical transport normal to the direction of transport. Since the circumferential and radial potential gradients remain in the same direction, the equivalent resistance of the two-dimensional cell circuit may be calculated from individual segment resistances with series and parallel circuits.

#### 2.1.5. Energy balance

Heat transfer within the tubular SOFC is closely coupled with current distribution and gas species distributions as the EEA electrical conductivities are temperature dependent. Key modes of heat transfer involve convection along the cathode, anode, and air tube, radiation between the cathode and air tube, and radial and axial thermal conduction along all layers and the air tube. Due to symmetry the interface between the cell and other cells is adiabatic. Heat transfer with the surroundings and end-effects are not considered for the single-cell model. Assumptions are chosen to represent a balance between accuracy and computational complexity for use in system-level studies and are common with other researchers.

Researchers conducting detailed steady-state analysis have found that gas flow on the anode side is within the laminar regime whereas flow on the cathode side lies within the transition region [21,22]. Convection heat exchange is calculated as a function of the heat transfer coefficient and the temperature difference between gas and solid temperatures as shown in Eq. (17):

$$Q_{conv,ij} = \sum_j h_j A_j (T_{s,surf,ij} - T_{g_i}) \quad [\text{W}], \quad (17)$$

with the total heat transfer to the gas denoted by  $Q_{conv,ij}$ , the solid surface temperature  $T_{s,surf}$ , and  $i$  and  $j$  refer to gas volume and solid volume respectively. Campanari used constant Nusselt numbers averaged along the axial length of the fuel cell solid–gas interfaces, and the same convention is applied here as calculated by Campanari [22].

Due to high operating temperatures near  $1000^\circ\text{C}$  and significant temperature differences between cell surfaces, radiation should be considered between the cathode inner radius and air tube outer radius. No radiation from the anode outer radius is considered due to the adiabatic boundary between cells in the single-cell model. The view factor from the inner air tube is unity while the view factor from the outer cathode is 0.3. Total radiation by heat transfer is calculated using the grey body radiation equation shown in Eq. (18):

$$Q_{rad,ij} = \varepsilon A_i F_{ij} \sigma (T_i^4 - T_j^4) \quad [\text{W}], \quad (18)$$

with the emissivity  $\varepsilon$  chosen as 0.8 in accordance with Stiller [27]. Radiation is only considered between opposing volumes; exchange between diagonal volumes is significantly less due to the high aspect ratio that results from discretizing the model into ten volumes.

The gas energy balance applies to the fuel chamber, the inner air chamber, and the outer air chamber. The thermal capacitance of the air and fuel is lower by  $10^{-1}$  to  $10^{-2}$  than the thermal capacitance of the solid, and the gas flow velocity is an order of  $10^2$  times the number of discrete segments which suggest the QSS is valid for the time step of interest, one second. The gas energy balances are modeled as QSS balances as shown in Eq. (19):

$$\dot{N}MWc_pT_{g|i,out} = \dot{N}MWc_pT_{g|i,in} + \sum_j h_j A_j (T_{s,surf,ij} - T_{g_i}) - \sum_k \Delta H_{ik} r_{ik}, \quad (19)$$

with the total molar flow rate of the finite volume  $\dot{N}$  in mol/s, the gas temperature  $T_g$  in K, the solid surface temperature  $T_{s,surf}$ , the combined mixture molecular weight  $MW$ , the reaction rate  $r$  in mol/s,  $i$  as an axial index for the finite volumes,  $j$  as a radial index for the solid surfaces surrounding the chamber, and  $k$  as an index for the reactions. Fourier's law of heat conduction is applied in the radial direction to model the conductive resistance between the solid temperature located in the center of the finite volume and the surface.

The mixture molecular weight,  $MW$ , is calculated as a sum of the individual species molecular weights weighted by the mole fraction,  $X_i$ , corresponding to each species as shown in Eq. (20):

$$MW = \sum_i MW_i X_i \quad (20)$$

$$X_i = \frac{\dot{N}_i}{\dot{N}}.$$

The specific heat capacities are calculated as a function of temperature using a constant pressure equation of state. A polynomial expression for the species is used in the form shown in Eq. (21):

$$\frac{c_{p,ig}}{R} = \alpha + \beta T + \gamma T^2 + \frac{\zeta}{T^2}, \quad (21)$$

with the coefficients  $\alpha$ ,  $\beta$ ,  $\gamma$  and  $\zeta$  dependent on the species [29] and  $c_{p,ig}$  and  $R$  in terms of  $J \text{ mol}^{-1} \text{ K}^{-1}$ .

The dynamic energy balance for the solid layers of the fuel cell, the anode, electrolyte, cathode, and air tube, are separately modeled to capture the slow thermal response having a time frame of hours. The dynamic solid layer energy balance is a function of heat and mass convection, heat conduction, and radiation. In addition, the electrolyte layer has a heat of reaction term. The generic energy balance is shown in Eq. (22):

$$\rho V c_{p,i} \frac{dT_{s,i}}{dt} = hA(T_{s,surf,i} - T_{g_i}) + kA \frac{dT_{s,i}}{dx} + \varepsilon F_i \sigma A (T_{s,opp}^4 - T_s^4) |i + Q_{elec}, \quad (22)$$

with the electrochemical exothermic heat release,  $Q_{elec}$ , only applied to the electrolyte layer, the radiation term only applied to the cathode and air tube layers, the index for layer  $s$ , and the index for volume  $i$ .

The exothermic heat release from electrochemical reactions is calculated as the difference between the potential power as the heat of reaction and the realized power produced by the cell as shown in Eq. (23):

$$Q_{elec} = \left( \frac{\Delta H_{f,H_2O(g)}}{nF} - V_{cell} \right) \cdot i \quad [\text{W}], \quad (23)$$

with the heat of steam formation  $\Delta H_{f,H_2O(g)}$  nearly constant versus temperature over the operating range.

### 2.1.6. Momentum balance

A steady-state momentum balance is applied to update the density and pressure for the fuel and air chambers as a function of system temperature. Pressure drop in the system has been considered to be approximately two-percent [23], and the model here assumes constant pressure along each chamber since a linear interpolation of the end pressure drops showed negligible effect on other properties. Consistent with all equipment models, the SOFC model calculates pressure using a downstream pressure as a model input. The pressure drop from chambers to downstream pressure is calculated as a function of frictional head loss. The equations involved in calculating the three SOFC pressures,  $p_{fuel}$ ,  $p_{air,1}$ , and  $p_{air,2}$ , are shown as follows:

$$\rho_j = \frac{p_d}{R_g T_{j,avg}} \quad [\text{kg m}^{-3}], \quad (24)$$

$$v_j = \frac{\dot{m}_j}{\rho_j A_j} \quad [\text{m s}^{-1}], \quad (25)$$

$$\mu_j = \alpha T_{j,avg} + \beta \quad [\text{Pa s}], \quad (26)$$

$$p_j = p_d + \frac{f L v_j^2}{2 D_h} \quad [\text{Pa}], \quad (27)$$

with the density  $\rho$ , downstream pressure  $p_d$ , gas constant  $R_g$  [ $\text{J kg}^{-1} \text{ K}^{-1}$ ], average chamber temperature  $T_{avg}$ , velocity  $v$ , mass flow rate  $\dot{m}$ , flow area  $A$ , viscosity  $\mu$ , friction factor  $f$ , chamber length  $L$ , and hydraulic diameter  $D_h$ . The viscosity expression is an empirical fitting of temperature-dependent data.

### 2.1.7. Controlled variables

The SOFC controlled variables are calculated from the mass, energy, and electrical balances and are comprised of the minimum cell temperature  $T_{electrolyte,min}$ , maximum radial thermal gradient  $\Delta T_{radial,max}$ , power  $P$ , fuel utilization  $U_f$ , air utilization  $U_a$ , and efficiency  $\eta_{LHV}$ . The minimum cell temperature is simply the minimum electrolyte temperature in the axial direction. The radial thermal gradients are calculated as the difference between the mean layer temperatures divided by the radial distance. The radial thermal gradient between the anode and electrolyte layers is shown in Eq. (28):

$$\frac{\Delta T_{sa-se}}{\Delta r} = \frac{|T_{sa} - T_{se}|}{0.5(thk_{sa} - thk_{se})} \quad [\text{K m}^{-1}]. \quad (28)$$

The gradient between the electrolyte and cathode is calculated in the same manner as Eq. (28). The power is the product of current and voltage,  $P = IV$ , with the current  $I$  as the sum of all individual currents in each axial segment. The fuel utilization is equal to the amount of fuel consumed with respect to fuel supplied in molar quantities per Eq. (29) [27]:

$$U_f = 1 - \frac{\dot{N}_{out,H_2} + \dot{N}_{out,CO} + 4\dot{N}_{out,CH_4}}{\dot{N}_{in,H_2} + \dot{N}_{in,CO} + 4\dot{N}_{in,CH_4}}. \quad (29)$$

Note that the fuel utilization equation requires stoichiometric coefficients. Air utilization is equal to the amount of oxygen consumed versus oxygen supplied and is calculated as shown in Eq. (30):

$$U_a = 1 - \frac{\dot{N}_{out,O_2}}{\dot{N}_{in,O_2}}. \quad (30)$$

Efficiency is calculated by comparing power produced to the lower heating value (LHV) of fuel supplied as shown in Eq. (31):

$$\eta_{LHV} = \frac{P}{H_{0,H_2} \dot{N}_{in,H_2} + H_{0,CO} \dot{N}_{in,CO} + H_{0,CH_4} \dot{N}_{in,CH_4}}. \quad (31)$$

## 2.2. Ejector submodel

Fuel cell ejectors operate as a mixer and avoid any moving parts by using the Venturi effect to recycle spent fuel flow with pure feed fuel flow. The spent fuel, secondary flow, is rich in steam at high temperatures and mixed with lower temperature, carbon-rich, primary feed fuel.

Primary flow is delivered at high pressure and low velocity from the fuel compressor, and primary flow is accelerated at the de Laval nozzle throat to sonic speed thereby converting pressure energy to kinetic energy. The primary flow further accelerates to supersonic speeds within the expander to the nozzle exit. Acceleration to sonic conditions at the primary fuel nozzle throat is important to produce choked flow thereby ensuring that the mass flow is dependent solely upon the upstream pressure, excluding a downstream pressure contribution. The entrained secondary flow accelerates from the entrance through the mixing chamber. The primary and secondary flows begin mixing at the mixing chamber entrance and are fully mixed at the outlet of the mixing chamber.

As a static component, the design of the ejectors is critical to produce the desired steady-state steam-to-carbon ratios, fuel flows, SOFC inlet temperature and pressure, and fuel and air utilization. The design is also important to provide dynamic control using the fuel inlet pressure or mass flow rate as an MV. In order to represent the ejector design, a steady-state one-dimensional ejector model is used, consistent with validated modeling approaches in literature [30,31]. This model differs from common ejector models for refrigeration applications; in particular, fuel cell applications mix hot gases rather than saturated vapor and require a much lower pressure increase in the recycled flow. The model also uses a two-dimensional function for velocity as presented by Zhu [30].

### 2.2.1. Input and output variables

The ejector submodel receives inputs upstream from the fuel cell: the secondary gas temperature, pressure and mole fractions. The primary fuel gas temperature, pressure, and mole fractions are external MVs. The ejector calculates the mixed fuel temperature, pressure, and mole fractions as outputs sent to the prereformer submodel, and the steam-to-carbon ratio is calculated as an external CV.

### 2.2.2. Model equations

The ejector model is based upon model derivations by Zhu [30]. The equations may be grouped to calculate the primary states such that all equations within each group are solved simultaneously and implicitly, but groups of equations are solved sequentially, or explicitly. A full treatment of the ejector model is provided in published literature [30,32].

The SCR is calculated based upon exit conditions from the ejector as shown in Eq. (32).

$$SCR = \frac{\dot{N}_{H_2O}}{\dot{N}_{CH_4} + \dot{N}_{CO}} \quad (32)$$

This calculation of SCR is consistent with published literature [27,30].

## 2.3. Prereformer submodel

### 2.3.1. Modeling approach and assumptions

The prereformer breaks down higher hydrocarbons than methane and converts a portion of methane to hydrogen. The reformer is modeled as an adiabatic reactor with the heat necessary for reactions provided by the inlet fuel. A QSS assumption can be used since the states, temperature and mole fractions, are gas properties, consistent with the SOFC and ejector models. The lumped

approximation is used since local temperature calculations within the prereformer are unnecessary.

### 2.3.2. Input and output variables

Upstream temperature, mass flow, mole balances, and system pressure comprise the input variables to the prereformer, and all inputs besides the pressure are provided by the ejector submodel. The prereformer submodel calculates the temperature, mole fractions, and mass flow resulting from the endothermic reformation reactions.

### 2.3.3. Model equations

The prereformer lumped model calculates the outlet fuel temperature and mole fractions by evaluating steady-state material and energy balances. The material balance is evaluated with the same approach as the SOFC material balance as shown in Eq. (33):

$$\dot{N}_{i,out} = \dot{N}_{i,in} + \sum_j v_i r_j \quad [\text{mol s}^{-1}]. \quad (33)$$

The energy balance is composed of transport terms and endothermic generation from the reformation reactions as shown in Eq. (34):

$$\dot{N}MWc_p T_{g|i,out} = \dot{N}MWc_p T_{g|i,in} - \sum_j \Delta H_{ik} r_{ik}. \quad (34)$$

The specific heat is calculated as a function of temperature as shown in Eq. (21), consistent with the SOFC submodel. The reaction model is composed of methanation and water–gas shift reactions identical to the SOFC reactions in Eq. (2). More detailed model descriptions are provided elsewhere [32].

## 3. Simulations

### 3.1. Steady-state simulations

The steady-state SOFC model is solved to provide the basis for a validated steady-state and dynamic model and provide insight into steady-state thermal gradients. The steady-state model uses a forty volume discretization compared to a ten volume discretization for the dynamic model; a comparison of results between the two levels of discretization demonstrated consistency between the models [32].

#### 3.1.1. Steady-state model validation

The SOFC model results are initially compared to results from Campanari's tubular SOFC 2D model as commonly cited in SOFC literature [22]; axial temperature and concentrations are validated versus Campanari due to insufficient simulation or experimental data elsewhere. The present model is designed after the tubular Siemens-Westinghouse design and obtains many parameters from Campanari. The present model calculates temperatures for each EEA layer whereas the Campanari model uses lumped solid temperatures. Since radiation is not included in the Campanari model, this initial version of the present model likewise neglects radiation.

The plot of steady-state temperature profiles shown in Fig. 3 match well with the Campanari temperature profile. Note that all plots in this paper refer to the 267.5 kWe SOFC plant with a nominal 3.5 bar operating pressure and power output near maximum capacity; a 120.7 kWe plant case is only used for validation versus plant operating data.

The shape of temperature profiles is driven by several thermal mechanisms. Heat generated by ohmic resistance peaks near the center of the cell where current generation is highest. Likewise, heat generation from the exothermic electrochemical redox reactions increases with increasing current. The inlet fuel temperature,

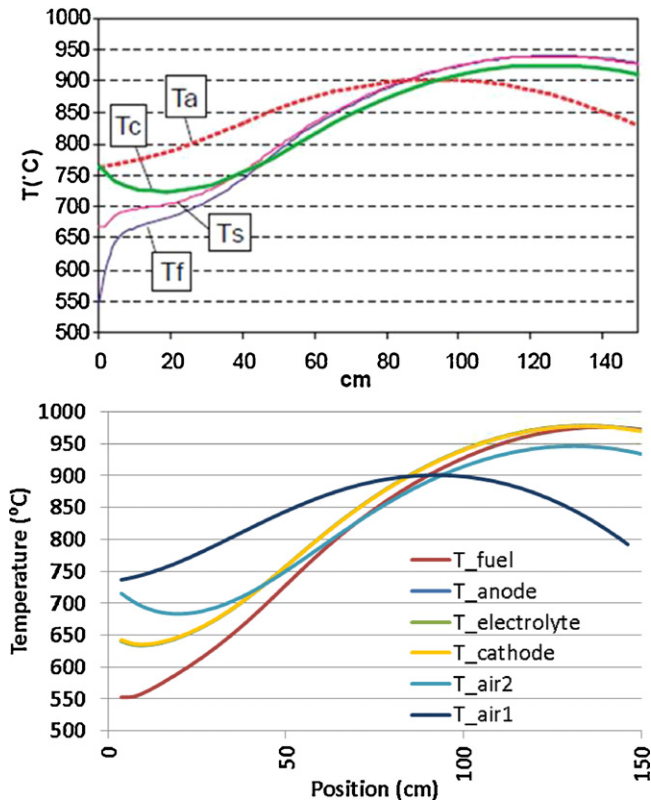


Fig. 3. Temperatures for Campanari [20] (upper) and the present model without radiation (lower).

$T_{fuel}$  is lower than the air temperature at the same axial location. Inlet air temperature,  $T_{air,1}$ , cools as it passes through an air supply tube which provides some thermal insulation from EEA solid temperatures,  $T_{anode}$ ,  $T_{electrolyte}$ , and  $T_{cathode}$ . The cathode-side air,  $T_{air,2}$ , converges towards the solid temperatures but later cools due to heat exchange with  $T_{air,1}$ . The solid air tube temperature, not shown because of the absence in Campanari's figure, exchanges heat via convection with both air temperatures. The temperature profiles demonstrate that the present model matches well with Campanari's model. The solid temperatures are most critical for SOFC reliability modeling, and the mean absolute percentage error for solid temperatures between the present model and Campanari's model is 3.85%.

Mole fraction profiles likewise match well with the Campanari mole fraction profile as shown in Fig. 4. Fuel flows from the left-side of the figure. The fuel mole fraction profiles illustrate the steam reformation of methane. Until the methane is fully consumed near 40 cm, the steam concentration decreases and the hydrogen concentration increases. Following methane consumption, these two concentrations pass through extrema points and then progress monotonically with decreasing hydrogen and increasing steam.

Differences between the present model without radiation and Campanari model may be explained by modeling differences relevant for thermal and chemical characterization, and several key equations, constants, and calibration variables are not provided by Campanari. Use of calibration factors for model fitting is limited to variables not provided by the literature used for validation: thermal contact resistance and fuel flow area between cells, and heat transfer coefficient multipliers. A thermal contact resistance factor exists to account for imperfect interfaces, material property variation, and microcracking. The outer diameter of the anode chamber in reality is not a concentric circle and difficult to model simply. A constant heat transfer coefficient is a simplifying assumption. The

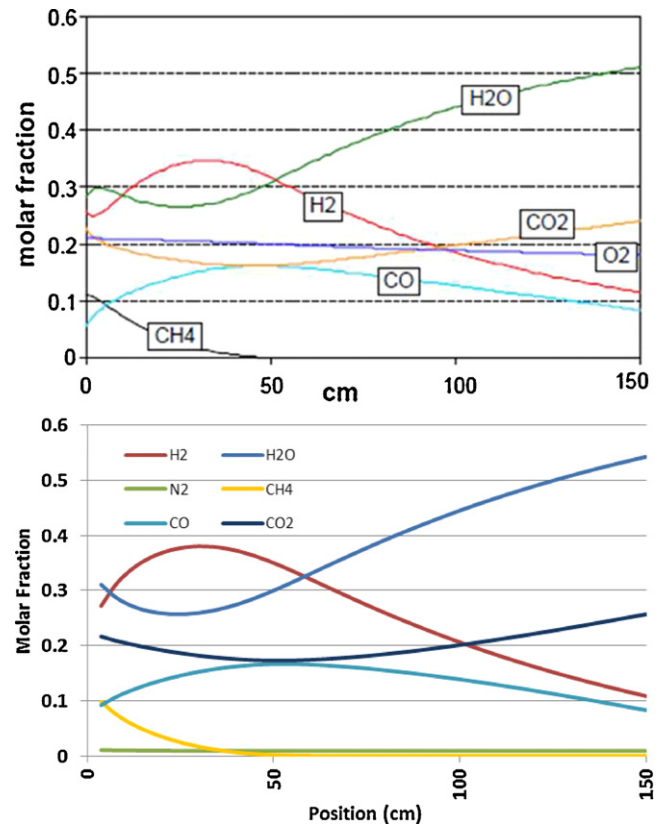


Fig. 4. Fuel mole fraction profiles for Campanari [20] (upper) and the present no-radiation model (lower).

comparison demonstrates that the present model without radiation matches well with Campanari's model.

While the present model uses many of the same parameters as Campanari, radiation between the concentric air supply tube and cathode cannot be neglected at the high SOFC operating temperatures as noted by other models [23]. SOFC steady-state results from the present model with radiation demonstrate that radiative heat transfer is  $10\times$  larger in magnitude than conductive and convective radial heat transfer, which have similar magnitudes. Radiation heat transfer must be included for accurate modeling and to verify the final present model versus plant data.

The steady-state temperature and mole fraction profiles for the present model with radiation demonstrate that including radiation makes a significant difference in overall SOFC operation. The temperature profile shown in Fig. 5 matches well with the temperature profile shown by Barzi with electrolyte temperatures at the peak temperature and at 150 cm are in close agreement though inlet conditions are not completely defined by Barzi [33]. The electrolyte temperature at the anode chamber inlet is much lower than results presented by Barzi since he uses pure hydrogen as fuel, thereby avoiding endothermic steam reformation reactions at the anode chamber inlet. The effect of radiation on mole fraction profiles is less significant than the effect on temperature profiles.

The common validation approach for tubular SOFC models in published literature is to compare model results for steady-state power, current density, voltage, fuel utilization, and air utilization versus plant operating results [22,23]. Two unique plants based on the Siemens-Westinghouse tubular SOFC design but having a different number of cells are run under different conditions. Plant A represents a 120.7 kWe SOFC plant comprised of 1152 cells operating at ambient pressure. Plant B represents a 267.5 kWe SOFC plant operating at 3.5 bar. Besides these values, the fuel and air



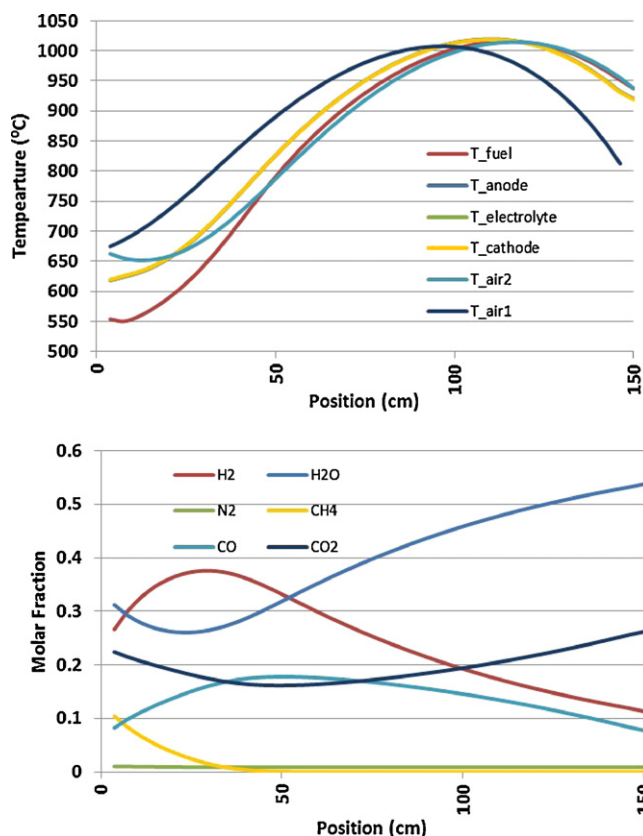


Fig. 5. Temperature and concentration profiles demonstrate the effect of radiation.

mass flows and cell voltage are provided as inputs from the plant data; Campanari estimates inlet fuel and air temperatures and inlet fuel concentration. Voltage, power, fuel utilization, and air utilization are compared versus plant and Campanari results as shown in Table 1.

The validation results illustrate that the present model with radiation matches the plant data within a similar accuracy as Campanari data. The present model is more accurate to plant data for all outputs in the pressurized SOFC case than the Campanari model with a maximum of 1.6% error for fuel utilization. Error in both the present model and Campanari model may be attributed to the absence of complete inputs from plant data, discretization, and modeling assumptions.

Thermal analysis of SOFC is important for reliability characterization with regards to microcracking and thermal fatigue. Radial

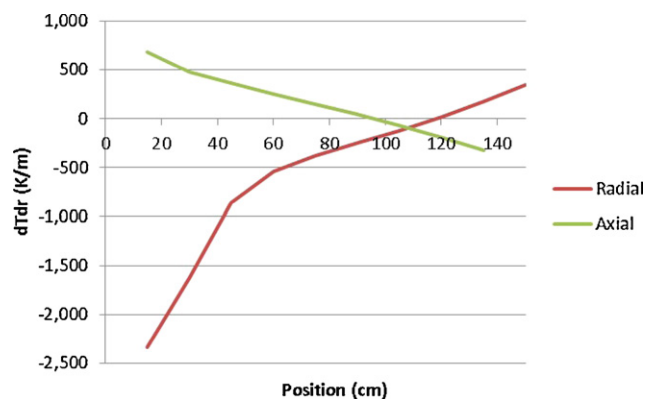


Fig. 6. Axial and radial thermal gradients along the SOFC length at nominal conditions.

thermal gradients have a higher magnitude in tension than axial thermal gradients for the tubular SOFC due to the fuel cell aspect ratio. The anode gas,  $T_{fuel}$ , temperature is over 100 K lower than cathode gas,  $T_{air2}$ , temperature at this location as shown in Fig. 5 thereby producing a negative radial thermal gradient. The anode and electrolyte will be placed in tension as the cathode thermally expands. As the barrier for charge transport, the electrolyte is particularly critical for cell lifetime.

The difference between the maximum radial thermal gradient in tension versus the maximum axial thermal gradient is significant as shown in Fig. 6. The maximum thermal radial gradient at nominal conditions is in excess of  $-2250$  K/mn whereas the maximum axial gradient remains below  $750$  K/m. Results by Fischer demonstrate a similar trend and magnitude for thermal gradients as those shown in Fig. 6 at the location of worst gradients and likewise demonstrate that the greatest radial gradient is between the anode and electrolyte [1]. Conditions that decrease the fuel inlet temperature and increase the air temperature near the fuel inlet will cause the radial gradient to increase further.

### 3.2. Dynamic simulations

Dynamic simulations of the SOFC system are performed for verification of the dynamic model, investigation of manipulated-controlled variable interactions, and characterization of the effect of disturbances on controlled variables. The dynamic model involves solving a dynamic tubular SOFC submodel and quasi-steady-state ejector and prereformer models at each time step. Open-loop dynamic simulations characterize the SOFC system settling time, the dynamic interaction of MVs and CVs, and the CV response to sinusoidal and step disturbances in methane fuel purity.

The dynamic simulations solve discretely at one second intervals in model time using MATLAB/Simulink. The dynamic SOFC submodel solves all states and parameters simultaneously using constrained nonlinear programming (NLP) optimization with APMonitor/APOPT as the modeling language/solver. The QSS ejector and prereformer submodels solve in MATLAB using the nonlinear least-squares algorithm *fsolve*.

#### 3.2.1. Dynamic model verification

Verification is the process of determining the degree to which the model accurately represents the intended description and specification for the model. Verification is unique from validation which involves confirming the model accurately represents real world phenomena. Many researchers in SOFC modeling have noted the absence of experimental data for validating dynamic SOFC models, and particularly the tubular SOFC [8,27]. However, many individual

Table 1  
Validation of the SOFC steady-state model with plant operating data.

Plant A	Model	Expected	% Error	Campanari % Error
Single cell power output (W)	109.0	104.8	4.0	1.6
Current density ( $A/m^2$ )	1792.0	1800.0	0.4	0.4
Voltage (V)	0.7294	0.6981	4.5	1.6
Fuel utilization (%)	68.4	69.0	0.8	0.6
Air utilization (%)	17.3	17.8	2.6	1.7
Plant B	Model	Expected	Error	Campanari error
Single cell power output (W)	158.0	157.0	0.6	3.0
Current density ( $A/m^2$ )	3000.0	3000.0	0.0	1.1
Voltage (V)	0.6315	0.6275	0.6	3.0
Fuel utilization (%)	70.1	69.0	1.6	2.9
Air utilization (%)	23.8	23.8	0.1	1.7

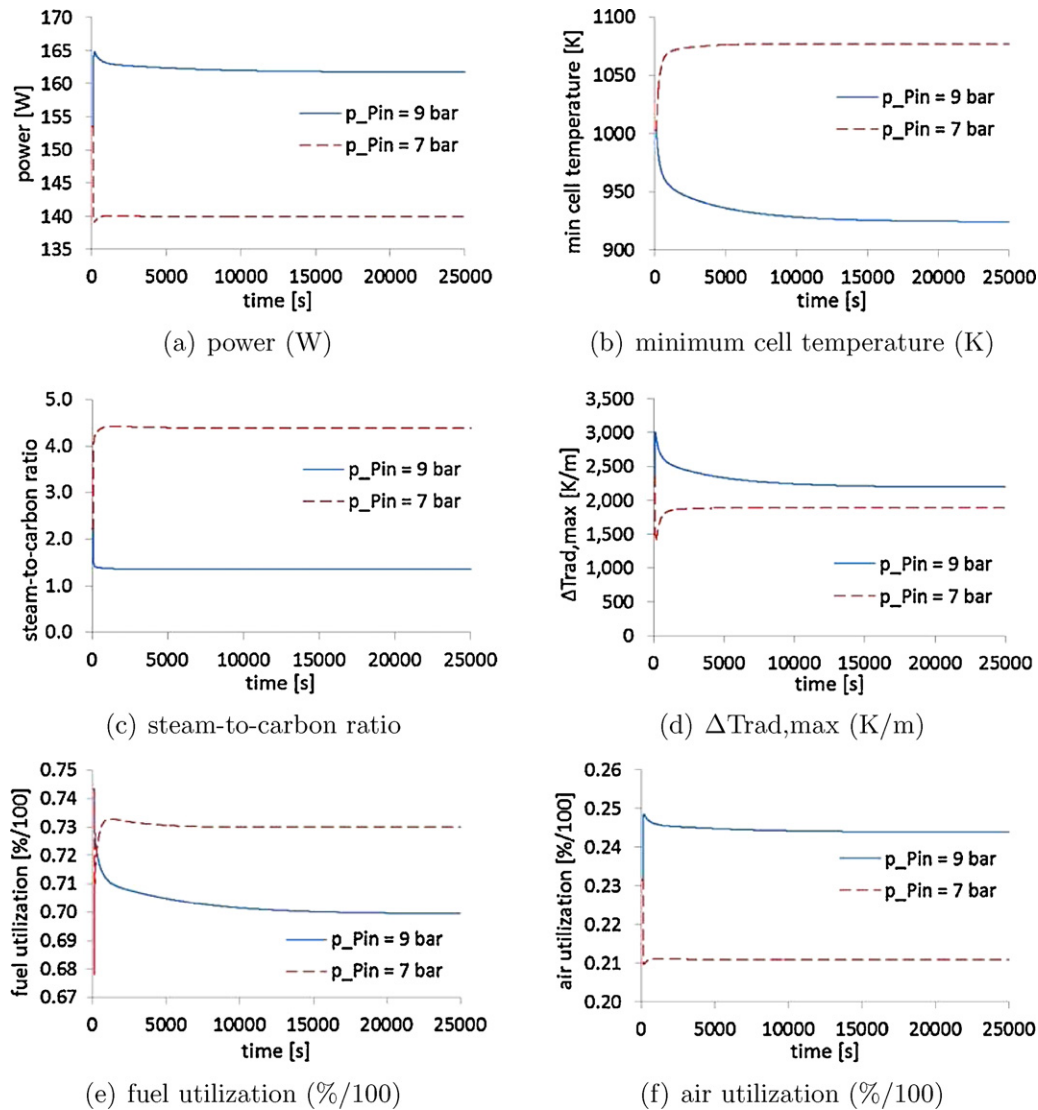


Fig. 7. Open-loop dynamic response to step changes in fuel inlet pressure.

equations used in SOFC modeling, such as chemical and electrochemical reaction rates, are based on empirically validated models, and many dynamic tubular SOFC models shown in literature have consistent settling times and dynamic MV–CV interactions. The model presented here meets specifications as follows: having a consistent dynamic response versus the body of published literature in dynamic SOFC modeling and having a sufficiently small spatial and temporal discretization to have a negligible effect on accuracy. Verification of the latter may be found in published work [32].

The open-loop dynamic response is examined by inducing an inlet fuel pressure step increase and decrease from the nominal  $8 \pm 1$  bar. The dynamic responses of the controlled variables, power, minimum cell temperature, steam-to-carbon ratio, radial thermal gradient, fuel utilization, and air utilization, are shown in Fig. 7.

The open-loop dynamic response of the CVs provides insight into the physical phenomena associated with SOFC operation. As fuel inlet pressure increases, the power likewise increases. The power response indicates both a fast and slow time constant suggesting numerator dynamics. For the step increase in fuel pressure, the power quickly reaches a maximum and then decreases with a slower, first-order approach to steady-state as shown in Fig. 7(a). The fast time constant is caused by the quick response of electrochemical reactions to changing fuel partial pressures. The slow time

constant is attributed to thermal inertia causing a longer-term drift in SOFC properties until thermal equilibrium is reached.

The minimum cell temperature undergoes a first-order decrease to steady-state as the power increases and demonstrates a 95% settling time of 9846 s for the step increase and 2038 s for the step decrease. The thermal settling time constant is consistent with literature referenced in this work. A key observation is that the minimum cell temperature moves inversely to power increases. As power increases, the fuel cell temperatures near the inlet and exit decrease while the maximum temperature increases producing a steeper axial profile. Since the cell temperature is constrained at a operability lower limit, increases in cell power may be limited by the temperature constraint.

The steam-to-carbon ratio likewise moves inversely to the power with a first-order rise or decline as seen in Fig. 7(c). The SCR demonstrates nonlinearity in how fuel pressure changes of equal magnitude cause an SCR response of differing magnitudes. The SCR will be an additional constraint when the controller moves to increase power from nominal.

Increasing power causes a direct increase in the maximum radial thermal gradient. This gradient demonstrates numerator dynamics similar to the power. The fast time constant for the maximum radial thermal gradient is a product of the quickly changing anode

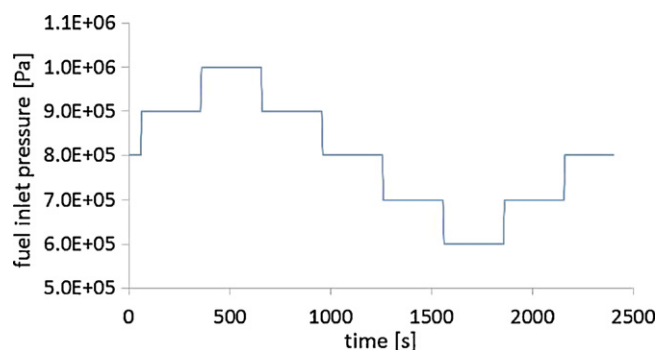


Fig. 8. The MV step change pattern used for the staircase dynamic simulations.

chamber thermal conditions. The step increase in fuel flow rate instantaneously decreases the anode ambient temperature. Since the maximum gradient occurs between the relatively thinner anode and electrolyte layers which are on the order of  $10^{-6}$  m thick, the maximum radial gradient increases instantaneously with the fuel pressure increase. As fuel cell EEA temperatures rise at a slower rate, the maximum gradient relaxes to a lower steady-state value. Since the maximum radial temperature gradient is constrained by an upper limit and increases simultaneously with power, it will be an additional constraint on power increases.

The dynamic response of fuel and air utilizations also exhibits numerator dynamics. The fuel utilization demonstrates a nonlinear response with differing dynamics for the fuel pressure increase and decrease. The increased fuel pressure and flow rate causes two phenomena that work together to decrease fuel utilization – an increased fuel consumption and power generation and a decreased cell temperature, which reduces reformation rates and increased ohmic losses. The air utilization moves in a similar manner as power with increased air utilization at a higher power level and vice versa.

### 3.3. Staircase tests for MV–CV interactions

Dynamic staircase tests are performed to aid in identifying the necessary control structure for advanced SOFC control. The staircase tests identify signs and magnitudes of MV–CV gains, assess nonlinearities, and characterize the type of dynamic response (e.g., first order or numerator dynamics, rise time, etc.). Staircase tests traverse a wider operating region than step tests and can therefore provide improved dynamic characterization, particularly regarding nonlinear interactions. Results from these tests justify the need for axial and radial discretization for control models and for controlling operability on the same time scale as power.

In the present work, the staircase tests are performed by making sequential step increases or decreases in each MV independently with a first-order hold over 5 s at 300 s intervals as shown in Fig. 8 for inlet fuel pressure; the pattern is identical for all MVs. Table 2 provides the size of MV step changes and highest and lowest values of the pattern. The step size is chosen to cover the feasible operating range of each MV actuator. For example, the inlet fuel temperature

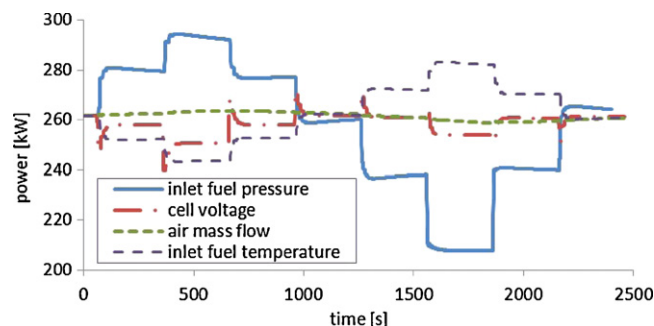


Fig. 9. Dynamic response of power to staircase changes in MVs.

is preheated with a recuperator, and thus room temperature is a reasonable lower limit for the fuel temperature MV. While the response of all MVs on the primary CVs is analyzed, only the most important MV–CV interactions are presented here.

The staircase tests identify the inlet fuel pressure and inlet fuel temperature as the primary MVs for controlling power generation as shown in Fig. 9. The inlet fuel pressure shows a direct relationship with power while the fuel temperature shows an inverse relationship. The pressure–power relationship has been explained previously in the open-loop settling time discussion. The power increases with lower fuel temperatures as the fuel becomes more dense at lower temperatures thereby increasing partial pressure. Voltage or current is often an MV for controlling power, but these variables become poor MVs as the current or voltage approaches the peak power at a given fuel and air flow rate as in this case. Air mass flow has a negligible effect on power.

Results of the absolute cell temperatures, Fig. 10 demonstrates that the inlet fuel pressure, inlet fuel temperature, and system pressure have the most significant effect on the minimum cell temperature. As power increases during  $t=0$  to 700 s and  $t=700$  to 1900 s, the minimum temperature, Volume 1, decreases; the minimum cell temperature consistently decreases with increasing power, and vice versa. Several effects contribute to this interaction: having a cooler fuel flow than air flow and the simultaneous flattening of temperature and current profiles. The effect of system pressure on power is similar but inverse to the effect of fuel pressure for similar reasons. The fuel temperature has a direct effect on the minimum cell temperature as expected. Another important conclusion from these plots is that the midpoint cell temperature at Volume 5 does not move parallel to the minimum cell temperature as shown in Fig. 10. This observation justifies the need for axial discretization and implies that the mean temperature is not ideal CV for reliability.

Plots of the maximum radial thermal gradients in Fig. 11 demonstrate numerator dynamics for the inlet fuel pressure, inlet fuel temperature, and system pressure MVs. The numerator dynamics are expected since step changes in these MVs produce an instantaneous change in convection heat exchange on the anode surface, and the maximum radial thermal gradient is responsive to small changes in anode and electrolyte temperatures; the gradient is less responsive to changing cathode-side conditions due to the cathode being one-thousand times thicker than the other two EEA layers. The slower time constant for the gradient occurs as the fuel cell approaches thermal equilibrium. Increases in fuel flow rate and decreases in fuel temperature produce a higher thermal gradient due to greater anode-side convection. The decreasing thermal gradient in response to increasing system pressure is attributed to the higher steam reformation rate producing more hydrogen, which has a specific heat several times other fuel species; note how this effect only occurs near the anode inlet before the reformation reaction is extinct. The air mass flow, air temperature, and cell voltage

Table 2  
Staircase test parameters for the manipulated variables.

Manipulated variable	Mean	Step size	Lowest value	Highest value
Inlet fuel pressure (bar)	8.0	1.0	6.0	10.0
Cell voltage (V)	0.6	0.04	0.55	0.71
Air mass flow (kg/s)	0.634	0.08	0.474	0.794
Air temperature (K)	1050.0	50.0	948.0	1150.0
Fuel temperature (K)	373.0	50.0	273.0	473.0
System pressure (bar)	3.5	0.45	2.6	4.4

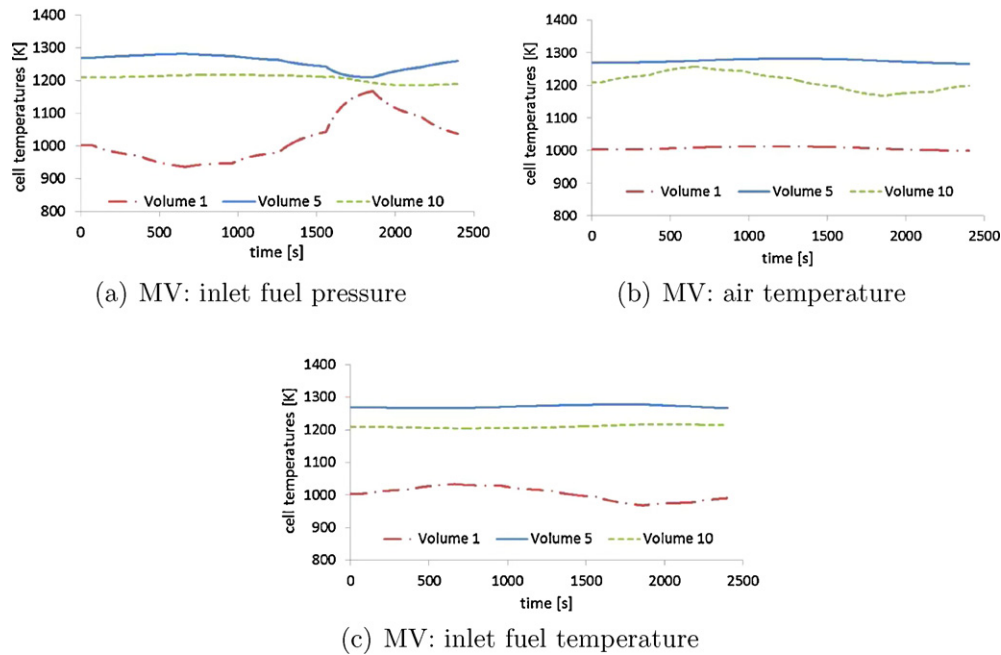


Fig. 10. Dynamic response of cell temperatures to staircase changes in MVs.

have an insignificant steady-state effect on the maximum radial thermal gradient. Air parameters have little effect on the gradient primarily due to cathode thermal insulation, and heat removal is primarily on the fuel side at the location where the maximum radial thermal gradient occurs. Some unusual gradient dynamics are due to the location of maximum radial thermal gradient shifting.

The steam-to-carbon ratio dynamics indicate that all MVs besides inlet air mass flow and inlet air temperature have a significant effect on the SCR. The SCR plots also demonstrate significant nonlinearities between the SCR and certain MVs, inlet fuel pressure and system pressure. Since the recommended minimum SCR is approximately 1.8–2.0, increasing power beyond nominal will place the SCR in an unsafe operating zone. The cell voltage has an inverse relationship with SCR due to the inverse relationship between voltage and current. The monotonic, inverse current–voltage relationship is demonstrated in Fig. 14 since  $U_a$  moves directly with current per the redox reaction. Hence, the fuel cell will produce less steam via the electrochemical reaction at higher voltages as seen in Fig. 12. Since higher temperatures lead to higher SOFC current, increasing the fuel temperature causes an increased SCR. Increasing the system pressure shows a significant increase in SCR, indicating that the system pressure is a good candidate for controlling SCR. The air mass flow and temperature have

a minimal effect on SCR in the timescale of interest due to ceramic insulation from the fuel stream.

The dynamic response of fuel utilization to staircase input steps, shown in Fig. 13, indicates that the cell voltage is the primary MV for controlling  $U_f$ ; the inlet fuel temperature and system pressure also have a significant effect. As discussed with the steam-to-carbon ratio plots, the cell voltage has a monotonic, inverse effect on cell current. Increasing the voltage will decrease current and thereby

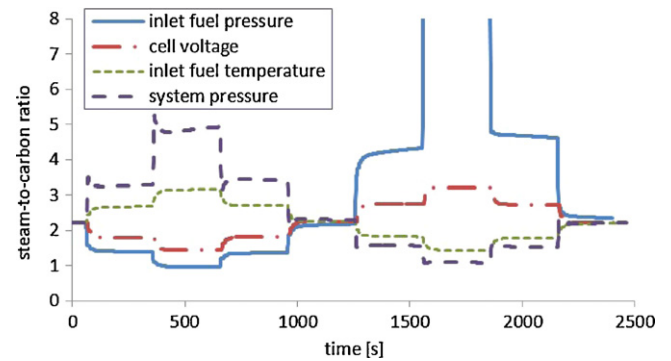


Fig. 12. Dynamic response of the steam-to-carbon ratio to staircase changes in MVs.

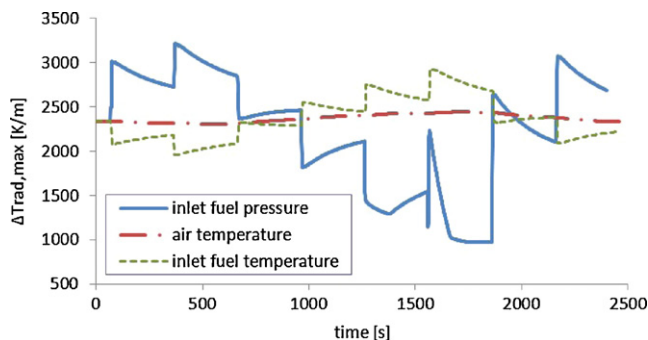


Fig. 11. Dynamic response of the maximum radial thermal gradient to staircase changes in MVs.

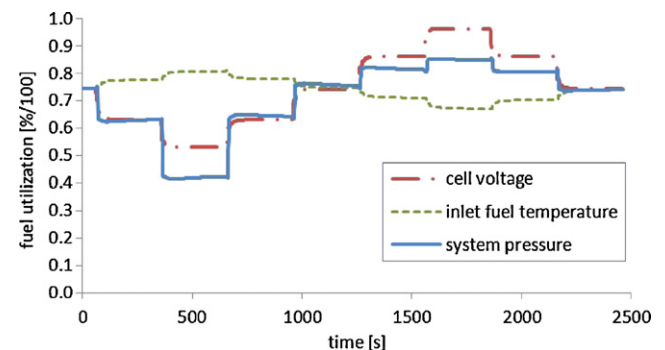


Fig. 13. Dynamic response of the fuel utilization to staircase changes in MVs.



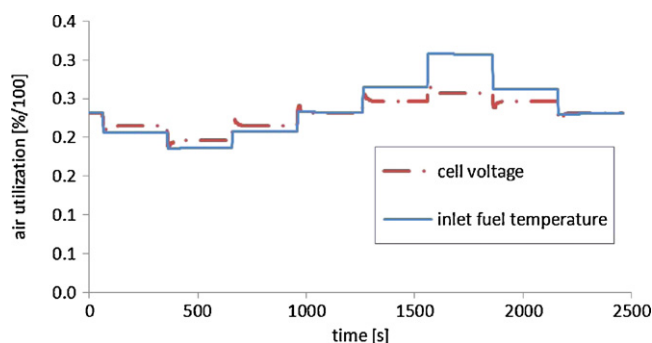


Fig. 14. Dynamic response of the air utilization to staircase changes in MVs.

decrease fuel utilization in a linear manner within the ohmic loss regime, and vice versa.

The response of air utilization corresponds linearly with current dynamics for all MVs besides  $m_{air}$  since oxygen depletion is linearly coupled to current generation. Fig. 14 demonstrates that air mass flow rate has the most significant effect on  $U_a$ . The inlet fuel pressure and cell voltage also have a significant effect on air utilization for control purposes. Air utilization is defined as the percent of oxygen flow depleted by the fuel cell during operation. Since the air mass flow rate has a negligible effect on power as shown in Fig. 9, increased air flow rate naturally increases the amount of undepleted oxygen exiting the fuel cell. In following with the current–voltage relationship already discussed in this section, increased voltage is expected to have a nearly linear effect on  $U_a$  although this effect diminishes at the lowest voltage, likely due to peak power being reached.

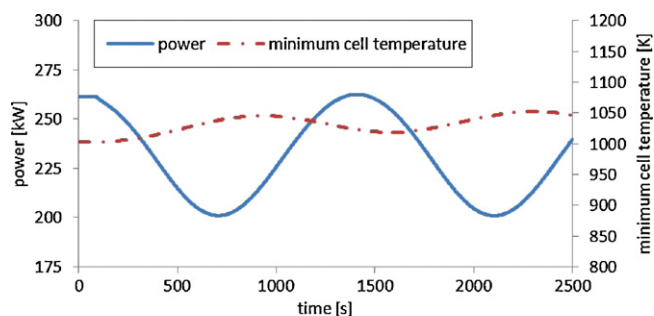
The dynamic plots for efficiency mirror those shown for the fuel utilization in Fig. 13 with different magnitudes and are shown in another work [32]. This coupling is expected due to the definition of fuel utilization and efficiency. As more fuel is utilized for a given amount of fuel provided, more power is produced relative to energy input.

Conclusions from the staircase tests are incorporated into the controller design. The dynamic analysis is critical to determine MVs that produce a significant and quick CV change. The air temperature has little dynamic effect on any CVs in the time frame of interest. The air mass flow primarily affects the air utilization, suggesting that the air mass flow is not needed to control other CVs. The plots demonstrate that increasing power without regard for other CVs will cause operability variables, the minimum cell temperature, maximum radial thermal gradient, fuel utilization, and the steam-to-carbon ratio, to reach or exceed their safe operating limits.

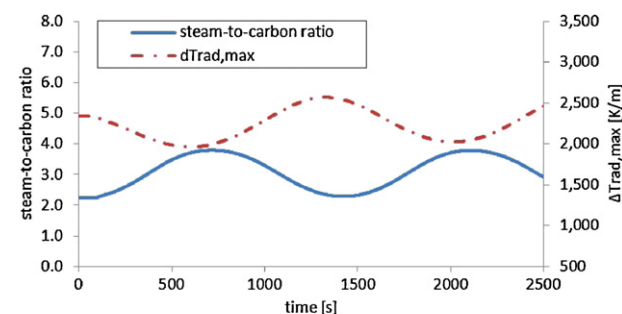
### 3.3.1. Fuel quality disturbance tests

The primary disturbance to SOFC operation is fuel quality variation. This disturbance is most likely to occur when the SOFC generates power for industrial applications, such as landfills, agriculture, chemical plants, and biofuel processing plants. In this example, natural gas produced as a biogas may contain  $CO_2$  concentration in the range of 40% before scrubbing and 20–30% after scrubbing [34]. Sinusoidal and step variations in  $CH_4$  and  $CO_2$  are sent to the plant during steady-state open-loop operation. The sinusoidal variation is equal to  $\pm 10\%$  from a nominal value of 90%  $CH_4$ , and the step size is a 15% decrease from the initial value of 100%  $CH_4$ .

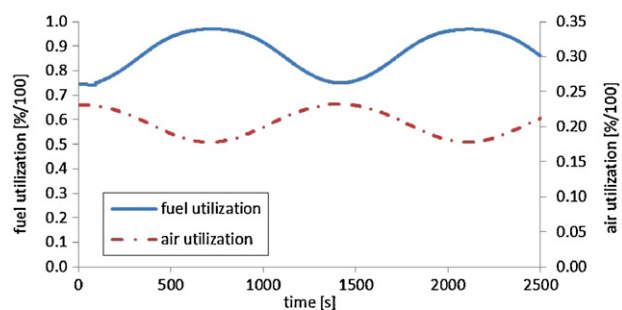
The purpose of the fuel quality disturbance tests is to assess how fuel quality variation affects the SOFC ability to satisfy load targets and operability constraints. The dynamic response of CVs to the fuel quality variation is shown in Fig. 15. The plots demonstrate that the valleys of  $CH_4$  concentration coincide with valleys in power, the



(a) power (W)



(b) steam-to-carbon ratio



(c) fuel utilization (%/100)

Fig. 15. Open-loop dynamic response to sinusoidal variation in fuel  $CH_4$  and  $CO_2$  concentration.

maximum radial thermal gradient, and air utilization, and peaks in the minimum cell temperature, SCR, and fuel utilization. The mean of the sinusoidal plots also show slight trends upwards or downwards. A decrease in 20%  $CH_4$  concentration causes a 60 kW<sub>e</sub>, or 23%, reduction in power output, and fuel utilization is in excess of 90%. Additional operability CVs will be constrained if the controller seeks to maintain power output with lower methane concentrations.

The step decrease in  $CH_4$  concentration by 15% causes a 44 kW<sub>e</sub>, or 17%, decline in power generation as shown elsewhere [32].

## 4. Model predictive MIMO control

Planning the control strategy for the SOFC in particular requires prioritization of control objectives, particular consideration for the SOFC design at hand, and understanding of the complex system dynamics and disturbances. Control of SOFC operation requires satisfying often competing performance and operability objectives. Load-following is the primary performance objective, and efficiency maximization may be a secondary performance objective. Operability goals primarily involve providing sufficient steam to prevent carbon deposition, ensuring thermal stresses do not cause premature fatigue or failure, and maintaining an adequate supply

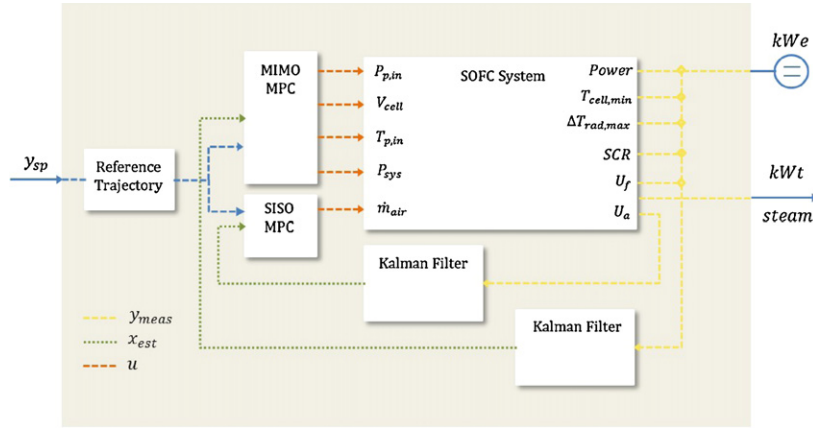


Fig. 16. The SOFC linear model predictive control system architecture.

of fuel and oxidant for redox reactions. The SOFC geometry, flow configuration, and inlet conditions are primary factors requiring unique controller design for the system at hand. For instance, the primary driver for thermal stress in the tubular SOFC, the minimum cell temperature, is correlated with sintering temperatures. The endothermic steam reformation reaction produces a thermal sink at either the inner or outer diameter of the tubular SOFC depending on flow configuration. The SOFC dynamics are characterized by nonlinear, multivariable interactions between manipulated and controlled variables driven by electrical, chemical, and thermal time constants with orders varying from milliseconds to hours. Finally, common SOFC disturbances are ambient temperature and fuel quality variation. Various applications, particularly using bio-gas feed, may produce varying fuel purity, and controller robustness to these disturbances is examined. For the present model, heat transfer to the ambient through stack walls is not considered since the model represents a cell in the stack center, and gas temperatures are controlled to mitigate the effect of ambient conditions on gas streams.

In consideration of the complex dynamic interactions, unique system configuration, and competing control objectives, the need for advanced control of SOFC is apparent. Model predictive control (MPC) is an ideal general advanced controller that provides capability for constrained, multivariable model-based regulatory and tracking control. Constrained control satisfies operability constraints with minimum effect on load-following, and multivariable models permit prediction of system dynamic responses.

#### 4.1. Controller design

The control system consists of two output feedback MPC controllers, one MIMO and one SISO. Two controllers are chosen because most MVs and CVs have multivariable interactions whereas  $\dot{m}_{air}$  has no effect on most CVs besides  $U_a$ . For this closed-loop system, all CVs are measured outputs, and the Kalman filter converges on these outputs to estimate the initial conditions for the model states as shown in Fig. 16. The Kalman filter is a standard algorithm and produces a linear unbiased minimum variance estimate. In a real system, some CVs, such as  $\Delta T_{rad,max}$ , will likely need to be calculated if not estimated using model-based estimation; the physical and empirical models used here to estimate  $\Delta T_{rad,max}$  likewise may be extended for state estimation. While other authors have decoupled the multivariable SOFC control problem, the simulation results demonstrated how operability CVs may have a similar dynamic response to the power CV. Thus, coupling all interacting MVs and CVs is necessary.

##### 4.1.1. Control model description

The control model is based upon a linear state-space model of ordinary differential equations (ODEs). The model as shown in Eq. (35) is multivariable and discretized at the control time step of 10 s:

$$\begin{aligned}\dot{x}_{n_x}(k+1) &= A_{n_x}x_{n_x}(k) + B_{n_x}u(k) \\ y(k) &= C_{n_x}x_{n_x}(k).\end{aligned}\quad (35)$$

The state-space model is derived from transfer function models, which are identified using the MATLAB System Identification Toolbox. The MISO transfer function model for each CV may be first- or second-order and may have numerator dynamics as shown in Eq. (36):

$$G(s) = \left[ \frac{K(\tau_a s + 1)}{(\tau_1 s + 1)(\tau_2 s + 1)} \quad \cdots \quad \frac{K(\tau_a s + 1)}{(\tau_1 s + 1)(\tau_2 s + 1)} \right]. \quad (36)$$

The sum of transfer function orders for all CVs determines the state-space model index,  $n_x$ . The transfer function model is identified from empirical pseudo-random signals that span the feasible control region. To aid identification the gain signs are constrained based upon expected behavior from step tests. Converting the transfer function to state-space form is trivial using inverse Laplace transforms.

Integral action is incorporated into the state-space model by forming an augmented state-space model as shown in Eq. (37):

$$\begin{aligned}\begin{bmatrix} \Delta x_{n_x}(k+1) \\ y(k+1) \end{bmatrix} &= \begin{bmatrix} A_{n_x} & 0_{n_x}^T \\ C_{n_x}A_{n_x} & I_{n_y} \end{bmatrix} \begin{bmatrix} \Delta x_{n_x}(k) \\ y(k) \end{bmatrix} + \begin{bmatrix} B_{n_x} \\ C_{n_x}B_{n_x} \end{bmatrix} \Delta u(k) \\ y(k) &= \begin{bmatrix} 0_{n_x} & I_{n_y} \end{bmatrix} \begin{bmatrix} \Delta x_{n_x}(k) \\ y(k) \end{bmatrix}.\end{aligned}\quad (37)$$

Integral action is necessary to eliminate the steady-state offset in closed-loop control due to plant-model mismatch.

##### 4.1.2. MPC formulation

The model predictive controller is formulated as an NLP and solved using the MATLAB *fmincon* interior-point solver. The objective function is formed to minimize the output error while suppressing control moves and suppressing use of slack variables as shown in Eq. (38):

$$\min_{u(t)} J = \frac{1}{2}(\mathbf{y} - \mathbf{y}_{ref})^T \mathbf{Q}(\mathbf{y} - \mathbf{y}_{ref}) + \frac{1}{2}\Delta \mathbf{u}^T \mathbf{R} \Delta \mathbf{u} + \frac{1}{2}\xi^T \mathbf{V} \xi, \quad (38)$$

where  $\mathbf{y}$  is the vector of CVs at all prediction time steps,  $\mathbf{y}_{ref}$  is the reference trajectory,  $\Delta \mathbf{u}$  is the change in MV between each control time step, and the slack variables are defined commonly as  $\xi \geq 0$ . Slack variables are included to provide soft constraints on  $\mathbf{y}$  bounds. Values for the weight matrices  $\mathbf{Q}$ ,  $\mathbf{R}$ , and  $\mathbf{V}$  are chosen heuristically

to provide a monotonic change in power with minimal overshoot for all CVs from their target or constraint.

The objective function as shown in Eq. 38 is further described as a function of state variables as shown in Eq. (39):

$$\min_{\mathbf{u}(t)} J = \frac{1}{2}(\mathbf{x} - \mathbf{x}_{ref})^T \tilde{\mathbf{Q}}(\mathbf{x} - \mathbf{x}_{ref}) + \frac{1}{2} \Delta \mathbf{u}^T \mathbf{R} \Delta \mathbf{u} + \frac{1}{2} \xi^T \mathbf{V} \xi, \quad (39)$$

where

$$\mathbf{x} - \mathbf{x}_{ref} = (\Gamma \Delta \mathbf{u} + \Omega \mathbf{x}_0) - \tilde{\mathbf{C}} \mathbf{y}_{ref}, \quad (40)$$

and  $\tilde{\mathbf{C}}$  is a block diagonal matrix of  $\mathbf{C}^{-1}$  and  $\Gamma$  is derived directly from Eq. (37). Substitution of Eq. (40) into Eq. (39) causes the objective function to be nonlinear.

Constraints on the MVs and CVs ensure that the optimal solution to Eq. (38) lies within the feasible region. Two types of MV constraints exist in this work. Actuator operating limits constrain overall actuator travel, and delta limits set a maximum limit on  $\Delta \mathbf{u}$ . Both may be incorporated as hard limits (i.e., without slack variables). CV constraints are critical to remain within the safe operating region for extending SOFC lifetime; these are incorporated as soft constraints to prevent NLP infeasibilities as shown in Eq. (41).

$$\begin{aligned} \mathbf{u}_{min} &\leq \mathbf{u}(k) \leq \mathbf{u}_{max} \\ \Delta \mathbf{u}_{min} &\leq \mathbf{u}(k) - \mathbf{u}(k-1) \leq \Delta \mathbf{u}_{max} \\ \mathbf{y}_{min} &\leq \mathbf{y}(k) + \xi(k) \leq \mathbf{y}_{max} \end{aligned} \quad (41)$$

For the case when the disturbance is modeled, the  $\Delta \mathbf{u}(k)$  vector is augmented to include the measured disturbance,  $\mathbf{x}_{CH_4}$  as shown in Eq. (42):

$$\Delta \tilde{\mathbf{u}}(k) = \begin{bmatrix} \Delta \mathbf{u}(k) \\ \Delta d(k) \end{bmatrix}. \quad (42)$$

The instances of  $\Delta \mathbf{u}(k)$  are replaced by  $\Delta \tilde{\mathbf{u}}(k)$  for the model prediction but not for constraint calculation.

#### 4.1.3. Reference trajectory

To provide for gradual, near monotonic setpoint tracking, the  $\mathbf{y}_{sp}$  is filtered to produce  $\mathbf{y}_{ref}$ . When the higher level controller or operator provides a new load setpoint, the governor recalculates the reference trajectory according to a first-order transfer function as shown in Eq. (43):

$$\mathbf{y}_{ref} = \mathbf{y}_0 + \mathbf{y}_{sp} \left( 1 - \exp \left( -\frac{t}{\tau_r} \right) \right) \quad (43)$$

where  $\tau_r$  is a time constant chosen as a function of the prediction horizon and  $t \in [0, t_{ss}]$ .

#### 4.1.4. Analytical derivatives

To expedite the NLP solution, analytical derivatives of the objective function are provided to the solver. The analytic Jacobian is calculated via matrix calculus as shown in Eq. (44):

$$\begin{aligned} \frac{dJ}{d\tilde{\mathbf{u}}} &= \left[ \frac{dJ}{d\mathbf{u}}, \frac{dJ}{d\xi} \right] \\ \frac{dJ}{d\mathbf{u}} &= \left( (\mathbf{x} - \mathbf{x}_{ref})^T \tilde{\mathbf{Q}} \Gamma + \Delta \mathbf{u}^T \mathbf{R} \right) \frac{d\Delta \mathbf{u}}{d\mathbf{u}} \\ \frac{dJ}{d\xi} &= \xi^T \mathbf{V} \end{aligned} \quad (44)$$

#### 4.1.5. Output feedback state estimation

Because the MPC algorithm uses a linear control model, a standard Kalman Filter is sufficient for reproducing the state variables from output measurements. For linear systems the Kalman Filter provides a linear unbiased minimum variance estimate. A brief overview of the state estimation algorithm is provided here as a complete description of Kalman Filtering. The following algorithm

**Table 3**

Regulatory, tracking, and constraints settings for the MPC.

	Regulatory	Tracking	Upper limit	Lower limit
Power	Off	<b>On</b>	Off	Off
$\Delta T_{rad,max}$	Off	Off	<b>3000</b> K/m	Off
$T_{cell,min}$	<b>On/off</b>	Off	Off	<b>1000</b> K
$U_f$	Off	Off	<b>0.9</b>	Off
SCR	Off	Off	Off	<b>2</b>
$U_a$	Off	Off	<b>0.32</b>	Off

is iteratively performed at the current time for each measurement,  $j$ .

Taking the current time as  $t=k$ , the previous state vector,  $\mathbf{X}_0$ , and covariance matrix,  $\bar{\mathbf{P}}_0$ , at  $k-1$  is integrated forward to the current time to provide the *a priori* state estimation vector,  $\mathbf{X}^-$ , and covariance matrix,  $\bar{\mathbf{P}}$ , at time  $k$  as shown in Eq. (45):

$$\begin{aligned} \mathbf{X}^-(k)_j &= \mathbf{A}_j \mathbf{X}_0(k-1)_j + \mathbf{B}_j \Delta \mathbf{u}(k)_j \\ \bar{\mathbf{P}}(k)_j &= \phi_j \bar{\mathbf{P}}_0(k-1)_j \phi_j^T \\ \phi_j &= \mathbf{A}_j. \end{aligned} \quad (45)$$

The *a posteriori* state vector,  $\mathbf{X}^+$ , is calculated as the summation of  $\mathbf{X}^-$  and a correction term,  $\Delta \mathbf{x}(k)$ , based on the Kalman gain as shown in Eq. (46):

$$\begin{aligned} \mathbf{X}^+(k)_j &= \mathbf{X}^-(k)_j + \Delta \mathbf{x}(k)_j \\ \Delta \mathbf{x}(k)_j &= \mathbf{K}(k)_j \Delta \mathbf{y}(k)_j \\ \Delta \mathbf{y}(k)_j &= \mathbf{Y}(k)_j - \mathbf{G}(k)_j \\ \mathbf{G}(k)_j &= \mathbf{C}_j \mathbf{X}^-(k)_j, \end{aligned} \quad (46)$$

where  $\mathbf{Y}(k)_j$  is the measurement  $j$  at time  $k$  and  $\mathbf{G}(k)_j$  is the measurement variable calculated from state estimates.

The Kalman gain,  $\mathbf{K}$ , is calculated directly from matrix algebra as shown in Eq. (47):

$$\begin{aligned} \mathbf{K}_j &= \bar{\mathbf{P}}(k)_j \tilde{\mathbf{H}}_j \left( \tilde{\mathbf{H}}_j \bar{\mathbf{P}}(k)_j \tilde{\mathbf{H}}_j^T \right)^{-1} + \mathbf{R} \\ \tilde{\mathbf{H}}_j &= \mathbf{C}_j, \end{aligned} \quad (47)$$

where  $\mathbf{R}$  is a weighting matrix chosen by the user, an identity matrix in this case the same for all measurements  $j$ . The state vector is updated  $j$  times, once for each measurement at the current time  $k$ .

#### 4.2. Closed-loop control results

The MPC controller described has been implemented in closed-loop with the dynamic SOFC plant as shown in Fig. 16. The MPC tracking objectives and constraints are set as shown in Table 3 unless otherwise noted. The MPC problem solves in 2 s using the MATLAB *fmincon* solver with a 4 GHz Pentium Core 2 Duo processor. This solution is within the sampling time of 10 s.

An initial study is performed to identify the prediction horizon tuning parameter. Power is the only tracking variable with all other CVs constrained at either an upper or lower limit. The prediction horizon study is performed by implementing step changes in  $\mathbf{y}_{sp}$  for power, an increase to 273 kW and decrease to 239 kW from a nominal 262 kW with a time step of 10 s; results are shown in Fig. 17. The results indicate that the MPC controller generally satisfies the control objectives for prediction horizons of 5, 10, and 20. However, the prediction horizon  $ph$  of 5 time steps produces less satisfactory results in several areas: (1) the load profile versus time exhibits oscillatory behavior; (2) some overshoot is seen on the load decrease, and (3) the steam-to-carbon ratio briefly violates the lower limit during the steep load increase. The prediction horizon must be sufficiently long to compensate for the slow time response of  $T_{cell,min}$ . The controller must foresee that  $T_{cell,min}$  is near

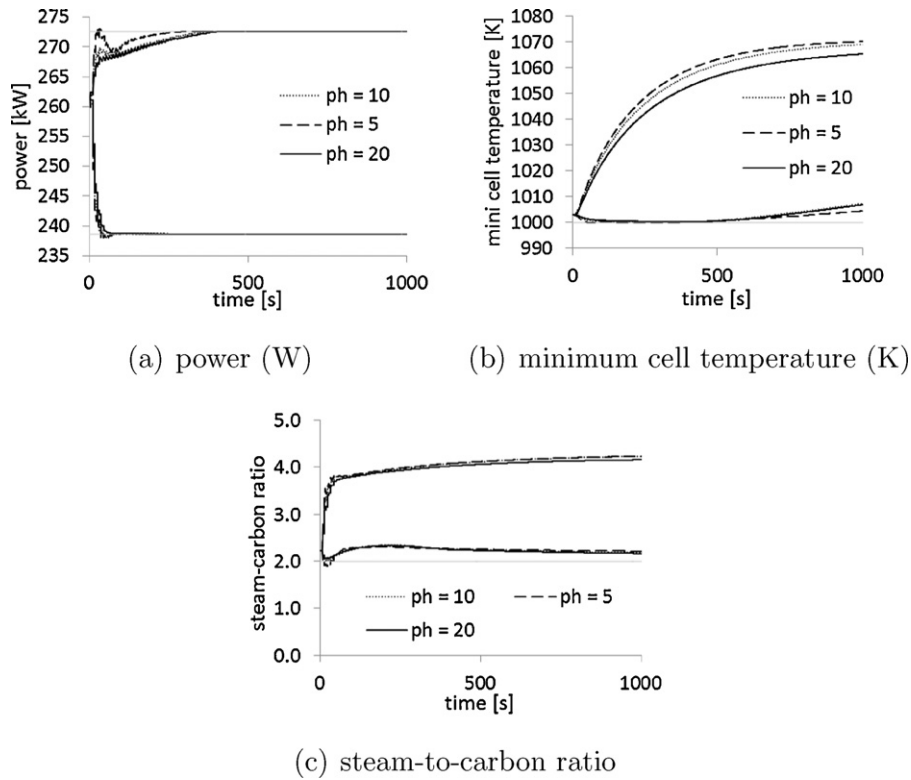


Fig. 17. Closed-loop load-following using different prediction horizons.

the lower limit, as with a prediction horizon of 10 or 20 to prevent drastic MV moves driven by the power following objective.

Common SOFC control strategies involve using a lumped dynamic simulator and controlling either a lumped (i.e., average) cell temperature or an outlet gas temperature without using constrained CV control. As noted already, a lumped model cannot capture two critical operability CVs for the tubular SOFC, the maximum radial thermal gradient and minimum cell temperature. Now,

the MPC algorithm is used to test whether controlling the average cell temperature provides satisfactory control of these two operability CVs. The outlet gas temperature has near identical dynamics to the average gas temperature as shown elsewhere [32]; thus including a test with outlet temperature tracking adds no additional value. This test is performed by using the following tracking variables: (1) power load, and (2) either minimum cell temperature or average cell temperature. To ensure only the average cell

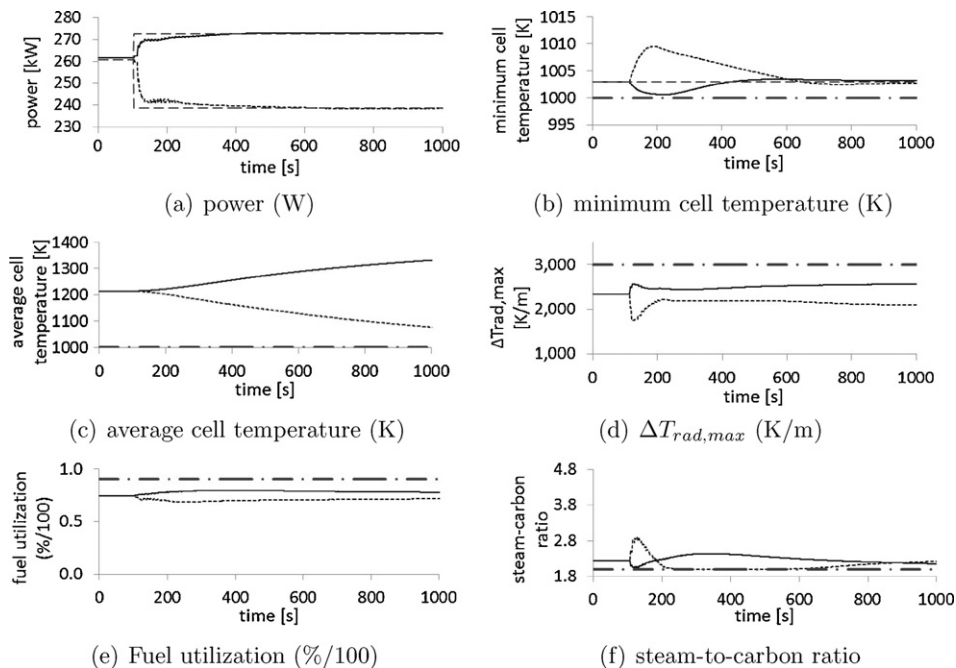


Fig. 18. Closed-loop power and minimum cell temperature tracking.



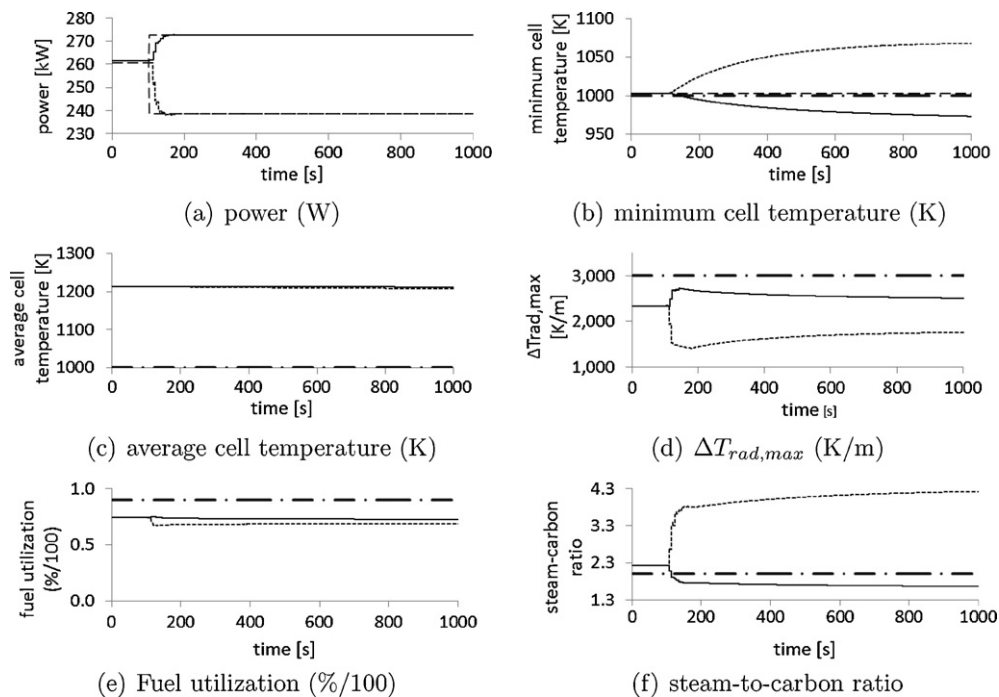


Fig. 19. Closed-loop power and average cell temperature tracking.

temperature tracking is affecting the minimum temperature profile and provide a better comparison with unconstrained control, all CV limit constraints are removed. Results for the CV profiles are shown in Figs. 18 and 19 for minimum cell temperature tracking and average cell temperature tracking respectively.

In the power and minimum cell temperature tracking case, the power monotonically increases to the setpoint while the minimum cell temperature and steam-to-carbon ratio are prevented from exceeding lower limit constraints as seen in Fig. 18. The minimum cell temperature is also held within a range of 10 °C while the mean cell temperature drifts over 100 °C from the initial value; however,

since the mean temperature has no direct effect on reliability, this controller meets operability objectives.

In the power and average cell temperature tracking case, the power likewise reaches the setpoint monotonically, but the minimum cell temperature travels between 30 and 60 °C from the initial value as seen in Fig. 19; the SCR also violates its lower limit since it is now unconstrained. Successful mean cell temperature tracking is demonstrated in Fig. 19(c). The maximum radial thermal gradient increases by approximately 500 K/m although the mean cell temperature is constant as seen in Fig. 19(d). The plots demonstrate that controlling the average cell temperature, or outlet gas

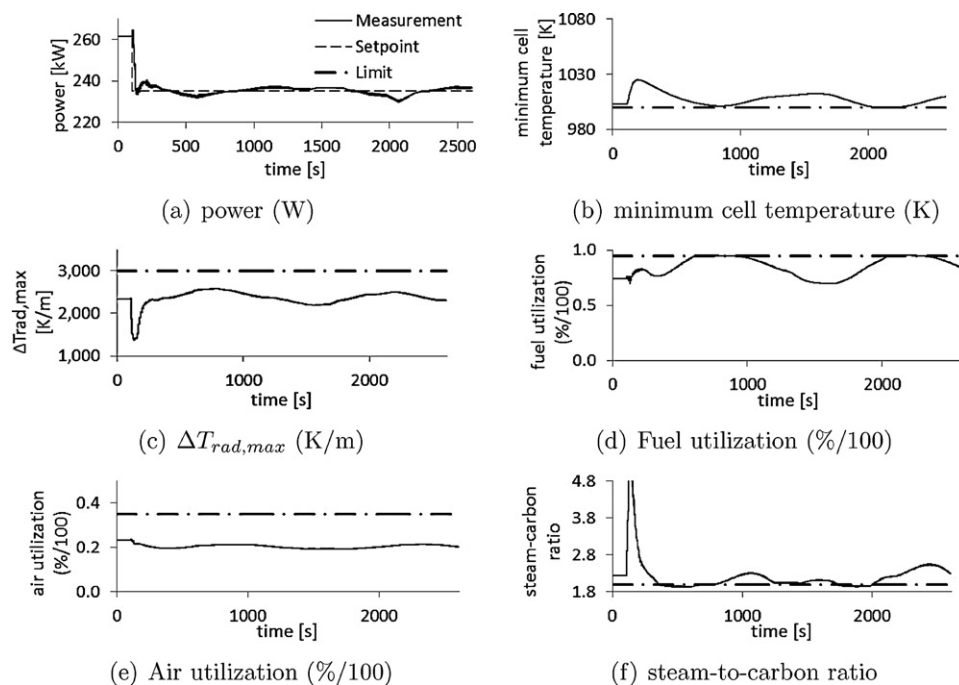


Fig. 20. Closed-loop load regulation with measured fuel quality disturbance rejection.

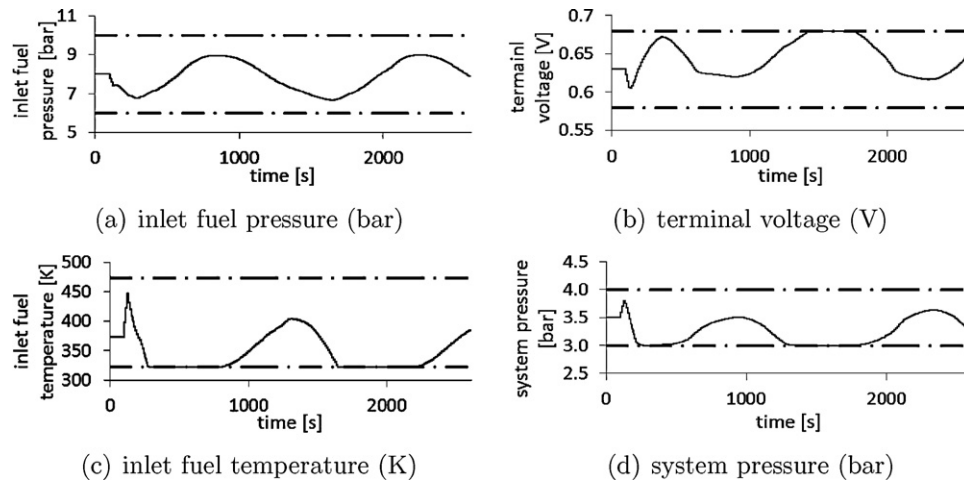


Fig. 21. MV profiles during closed-loop load regulation with disturbances.

Table 4

Integrated absolute error for setpoint tracking with disturbances.

Control case	Tracking variables	Disturbance model	Power IAE	$T_{cell,min}$ IAE
(1)	Power	None	4315	76,319
(2)	Power, $T_{cell,min}$	None	5808	8667
(3)	Power, $T_{cell,min}$	Included	4017	13,368

temperature, is not an effective means to controlling the two critical thermal stress drivers in the tubular SOFC. However, constrained control provides very effective operability control while adjusting MVs in an efficient manner (i.e., considering multivariable interactions and using MVs only as necessary to satisfy constraints, not unnecessary tracking).

The proposed model and MPC algorithm are tested for disturbance rejection capability with a sinusoidal fuel quality disturbance characterized by varying  $\text{CH}_4$  and  $\text{CO}_2$  concentrations. Three unique simulation cases are studied and the integrated absolute error (IAE) is compared in Table 4.

The controller with modeled disturbances succeeds at having the lowest IAE for load-following while including the minimum cell temperature as a tracking variable. All three cases have matching MPC tuning parameters – load tracking is weighted an order of magnitude larger than temperature tracking. The closed-loop controlled variable response with disturbances is shown for case 3 in Fig. 20. As the methane concentration reaches a minimum value near 700 s and 2100 s, the controller ability to maintain load is limited by the  $U_f$ , SCR, and  $T_{cell,min}$  CV constraints. In addition, three of the four MVs are riding upper or lower limits at various times as shown in Fig. 21. As the MPC finds optimal operation at MV limits for the inlet fuel temperature, system pressure, and voltage, an important conclusion from the MV plots is that the controller ability to meet operational objectives would be improved by expanding the MV ranges. Having an air compressor that operates at lower pressures would be beneficial while expanding the range of inlet fuel pressure would have little effect in this case. Including closed-loop control studies in the system design process would provide critical insight into the system's capability to meet performance and operability goals and predict capability to reject disturbances in potential new SOFC applications.

## 5. Conclusions

A dynamic, quasi-two-dimensional model for the tubular SOFC, along with ejector and prereformer models, is implemented using

APMonitor and MATLAB/Simulink and used in closed-loop control with a constrained model predictive control algorithm for controlling critical performance and operability variables. This work is novel in its approach in several ways:

- The thermal operability CVs are chosen based upon mechanical finite element analysis for cracking caused by excessive tensile stress.
- Thermal operability CVs, the maximum radial thermal gradient and minimum cell temperature, are modeled dynamically using a quasi-two-dimensional physics-based SOFC model.
- The dynamic SOFC model is solved simultaneously using the nonlinear programming optimization solver APOPT, without iteration between thermal and electrical equations.
- Open-loop and closed-loop multivariable analysis provides insight into the effects of all available MVs and CVs for tubular SOFC system control.
- A constrained, multivariable centralized controller is implemented to use the MVs in a more optimal manner to control CVs than decentralized unconstrained control.

The SOFC model is validated in the same manner as other tubular SOFC models [10,22].

Open-loop dynamic simulations provide insight into how the MVs affect the SOFC reliability. The inlet fuel temperature is seen to have a near immediate effect on the maximum radial thermal gradient whereas the air temperature has little effect – this can be explained due to the cathode-supported geometry. In addition, the results show that the two primary drivers for thermal stress occur near the fuel entrance, which is attributed to the endothermic steam reformation reactions. Staircase tests demonstrate that the inlet fuel pressure and inlet fuel temperature are primary MVs for controlling the fuel cell power and the voltage and system pressure have a significant effect on operability CVs.

Closed-loop MPC simulations demonstrate that conventional approaches to controlling SOFC thermal stress using a lumped or outlet gas temperature are not sufficient for the tubular SOFC. A control configuration that held the average cell temperature within several degrees C permitted the minimum cell temperature to travel over 100 K from nominal and the maximum radial thermal gradient to move 500 K/m towards the upper limit. MIMO constrained control is shown to be effective at performing load following and operability control even in the presence of sinusoidal disturbances of  $\pm 10\%$  methane concentration.

Future work should continue addressing the tubular SOFC control problem using constrained control with controlled variables chosen based on stress analysis. Additional work could incorporate a parameter estimation module for inferential control of the maximum radial thermal gradient and minimum cell temperature. We recommended the controller herein to be applied to investigate control of GT-SOFC hybrid systems, optimize system efficiency subject to disturbances and tight operability constraints, and investigate fault-detection scenarios.

## Acknowledgements

Tom Edgar writes in memory of Ken Muske, “I served as a member of Ken’s doctoral committee at The University of Texas at Austin and observed first hand his sharp mind as he and Jim Rawlings were developing the underpinnings of MPC. Aspentech developed a beta version of their MPC algorithm which they nicknamed the MR controller after Muske–Rawlings. Subsequently after Ken joined the faculty at Villanova, he and I wrote a book chapter on state estimation for the book by Henson and Seborg on Nonlinear Process Control. Ken and I also co-authored two papers on undergraduate and graduate process control education for the CPC7 conference in 2006. I highly valued my association with Ken before his untimely death. Ken will be dearly missed by all of us who knew him.”

The authors thank John Hedengren for assistance in providing and supporting the APMonitor Modeling Language for optimization of Differential and Algebraic (DAE) Models.

## References

- [1] K. Fischer, J. Seume, Impact of the temperature profile on thermal stress in a tubular solid oxide fuel cell, *Journal of Fuel Cell Science and Technology* 6 (2009) 1–9.
- [2] J.R. Ferguson, J.M. Fiard, R. Herbin, Three-dimensional numerical simulation for various geometries of solid oxide fuel cells, *Journal of Power Sources* 58 (1996) 109–122.
- [3] S. Kurachi, Y. Mizutani, T. Hiroyama, K. Katsurayama, F. Okada, K. Ukai, Development of a small-scale solid oxide fuel cell (SOFC), in: 24th World Gas Conference, Argentina, 2009.
- [4] A. Iyengar, N. Desai, S. Vora, L. Shockling, Numerical investigation of a delta high power density cell and comparison with a flattened tubular high power density cell, *Journal of Fuel Cell Science and Technology* 7 (2010) 1–8.
- [5] A. Hawkes, M. Leach, Solid oxide fuel cell systems for residential micro-combined heat and power in the UK: key economic drivers, *Journal of Power Sources* 149 (2005) 72–83.
- [6] S. Vora, Office of fossil energy fuel cell program – Solid State Energy Conversion Alliance (SECA) – clean economic energy for a carbon challenged world, in: 11th Annual SECA Workshop, Pittsburgh, PA, 2010.
- [7] J. Pierre, Siemens energy, in: 11th Annual SECA Workshop, Pittsburgh, PA, 2010.
- [8] D. Bhattacharyya, R. Rengaswamy, A review of solid oxide fuel cell (SOFC) dynamic models, *Industrial and Engineering Chemistry Research* 48 (2009) 6068–6086.
- [9] P. Aguiar, C. Adjiman, N. Brandon, Anode-supported intermediate-temperature direct internal reforming solid oxide fuel cell. II: model-based dynamic performance and control, *Journal of Power Sources* 147 (2005) 136–147.
- [10] C. Stiller, B. Thorud, O. Bolland, R. Kandepu, L. Imsland, Control strategy for a solid oxide fuel cell and gas turbine hybrid system, *Journal of Power Sources* 158 (2006) 303–315.
- [11] R. Kandepu, L. Imsland, B.A. Foss, C. Stiller, B. Thorud, O. Bolland, Modeling and control of a SOFC-GT-based autonomous power system, *Energy* 32 (4) (2007) 406–417.
- [12] F. Mueller, B. Tarroja, J. Maclay, F. Jabbari, J. Brouwer, S. Samuelsen, Design simulation and control of a 100 MW-class solid oxide fuel cell gas turbine hybrid system, *Journal of Fuel Cell Science and Technology* 7 (2010) 1–11.
- [13] F. Jurado, Predictive control of solid oxide fuel cells using fuzzy Hammerstein models, *Journal of Power Sources* 158 (2006) 245–253.
- [14] F. Mueller, F. Jabbari, J. Brouwer, S. Junker, H. Ghezal-Ayagh, Linear quadratic regulator for a bottoming solid oxide fuel cell gas turbine hybrid system, *Journal of Dynamic Systems, Measurement, and Control* 131 (2009) 1–9.
- [15] Y.L. Sun, S. Ghantasala, N.H. El-Farra, Networked control of distributed energy resources: application to solid oxide fuel cells, *Industrial & Engineering Chemistry Research* 48 (21) (2009) 9590–9602.
- [16] H. Huo, X. Zhu, W. Hu, H. Tu, J. Li, J. Yang, Nonlinear model predictive control of SOFC based on a Hammerstein model, *Journal of Power Sources* 185 (2008) 338–344.
- [17] M. Fardadi, F. Mueller, F. Jabbari, Feedback control of solid oxide fuel cell spatial temperature variation, *Journal of Power Sources* 195 (2010) 4222–4233.
- [18] S.J. Qin, T.A. Badgwell, A survey of industrial model predictive control technology, *Control Engineering Practice* 11 (7) (2003) 733–764.
- [19] J. Kent, Kent and Riegel’s Handbook of Industrial Chemistry and Biotechnology, 11th edition, Springer, 2007.
- [20] S. Campanari, Thermodynamic model and parametric analysis of a tubular SOFC module, *Journal of Power Sources* 92 (2001) 26–34.
- [21] P. Aguiar, C. Adjiman, N. Brandon, Anode-supported intermediate temperature direct internal reforming solid oxide fuel cell. I: model-based steady-state performance, *Journal of Power Sources* 138 (2004) 120–136.
- [22] S. Campanari, P. Iora, Definition and sensitivity analysis of a finite volume SOFC model for a tubular cell geometry, *Journal of Power Sources* 132 (2004) 113–126.
- [23] C. Stiller, B. Thorud, S. Seljebo, O. Mathisen, H. Karoliussen, O. Bolland, Finite-volume modeling and hybrid-cycle performance of planar and tubular solid oxide fuel cells, *Journal of Power Sources* 141 (2005) 227–240.
- [24] E. Achenbach, E. Riensche, Methane/steam reforming kinetics for solid oxide fuel cells, *Journal of Power Sources* 52 (1994) 283–288.
- [25] M. Hussain, X. Li, I. Dincer, A general electrolyte-electrode-assembly model for the performance characteristics of planar anode-supported solid oxide fuel cells, *Journal of Power Sources* 189 (2009) 916–928.
- [26] R. O’Hayre, S. Cha, W. Colella, F. Prinz, *Fuel Cell Fundamentals*, 2nd edition, Wiley, 2009.
- [27] C. Stiller, Design operation and control modelling of SOFC/GT hybrid systems, Doctoral thesis, Norwegian University of Science and Technology, 2006.
- [28] P. Costamagna, K. Honneger, Modeling of solid oxide heat exchanger integrated stacks and simulation at high fuel utilization, *Journal of Electrochemical Society* 145 (11) (1998) 3995–4007.
- [29] R. Perry, D. Green, *Perry’s Chemical Engineering Handbook*, 8th edition, McGraw-Hill Professional, 2007.
- [30] Y. Zhu, W. Cai, C. Wen, Y. Li, Fuel ejector design and simulation model for anodic recirculation SOFC system, *Journal of Power Sources* 173 (2007) 437–449.
- [31] F. Marsano, L. Magistri, A. Massardo, Ejector performance influence on a solid oxide fuel cell anodic recirculation system, *Journal of Power Sources* 129 (2004) 216–228.
- [32] B. Spivey, Dynamic modeling, model-based control, and optimization of solid oxide fuel cells, Ph.D. thesis, The University of Texas at Austin, 2011.
- [33] Y. Barzi, M. Ghassemi, M. Hamed, Numerical analysis of start-up operation of a tubular solid oxide fuel cell, *International Journal of Hydrogen Energy* 34 (2009) 2015–2025.
- [34] E. Porpatham, A. Ramesh, B. Bagalingam, Investigation on the effect of concentration of methane in biogas when used as a fuel for a spark ignition engine, *Fuel* 87 (2008) 1651–1659.